A LIKELIHOOD RATIO ALGORITHM FOR REMOVING LOCALIZED ALPHA PARTICLE BACKGROUNDS IN THE DEAP-3600 DETECTOR

by

Courtney Taylor Mielnichuk

A thesis submitted in partial fulfillment of the requirements for the degree of

Master of Science

Department of Physics
University of Alberta

Abstract

DEAP-3600 (Dark Matter Experiment using Argon for Pulse shape discrimination) is a single phase dark matter experiment using a tonne-scale mass of liquid argon as a target to observe spin-independent interactions with Weakly Interacting Massive Particles (WIMPs). Alpha decays from radioactive nuclei accumulating on the surface of detector materials are a background concern for the experiment. Specifically, alpha decays occurring in the neck region of the detector produce signals with characteristics similar to those expected for WIMP interactions. In order to estimate the potential background from alpha decays in the detector neck, projected material radioactivity levels have been incorporated into Monte Carlo simulations. A likelihood ratio algorithm to discriminate between neck alpha decays and a WIMP signal has been developed based on Monte Carlo simulation. The benefit of implementing a likelihood ratio cut, both in comparison and in combination with a fiducial volume cut, has been studied. Preliminary results of the likelihood ratio applied to commissioning data are also studied.

Acknowledgements

I would like to express my sincere gratitude to all of the people who have assisted and supported me in completing this degree.

Thank you to my supervisor, Aksel Hallin, for the opportunity to be a part of the DEAP collaboration, for sharing your knowledge and experience with me, and for your patience and cheerful nature. Thank you to Berta, James and Thomas for all of the time you have spent patiently assisting me, as well as to all of the members of the DEAP collaboration.

I would also like to thank my officemates, roommates and friends. I am more appreciative of your friendships than I could possibly ever express. And lastly, to my family, thank you.

Contents

List of Tables

List of Figures

List of Abbreviations

List of commonly used abbreviations

α	Alpha particle (^{4}He nucleus)
AmBe	Amerecium-Beriium
^{39}Ar	Isotope of Argon
AV	Acrylic Vessel
β	Beta particle (electron)
Bq	Bequerel, 1 decay/second
DAQ	Data Aquisition
DEAP	Dark Matter Experiment using Argon for Pulse shape discrimination
DTM	Digitizer and Trigger Module
eV	Electronvolt, 1.602×10^{-19} C
eV_{ee}	Electron-equivalent energy
γ	Gamma ray (photon)
Gap C	Inner edge of inner flow guide
Gap B	Outer edge of inner flow guide, and inner edges of outer flow guide and piston ring
Gap A	Outer edges of outer flow guide and piston ring
GAr	Gaseous Argon
kg yr	Exposure unit
LAr	Liquid Argon
LET	Linear Energy Transfer
LNe	Liquid Neon
nm	Nanometer

LXe	Liquid Xenon
^{208}Pb	Lead-208
^{210}Pb	Lead-210
PE	Photoelectron
PMT	Photomultiplier Tube
^{210}Po	Polonium-210
ppm	Parts per million
ppb	Parts per billion
PSD	Pulse Shape Discrimination
RAT	Reactor Analysis Tool
^{220}Rn	Radon-220
^{222}Rn	Radon-222
ROI	Region Of Interest
SCB	Signal Conditioning Board
SD	Spin-Dependent interaction
SI	Spin-Independent interaction
^{232}Th	Thorium-232
TPB	1,1,4,4-Tetraphenyl-1,3-Butadiene
^{238}U	Uranium-238
WIMP	Weakly Interacting Massive Particle

List of Symbols

List of commonly used symbols

A	Atomic mass of target nucleus
A_{surf}	Activity of surface
a_n	Spin-independent coupling of a WIMP to a neutron
a_p	Spin-dependent coupling of a WIMP to a proton
c	Speed of light, 299 792 458 ms^{-1}
CO	Carbon monoxide
CO_2	Carbon dioxide
χ	Dark matter particle
CH_4	Methane
E_R	Recoil energy of a nucleus
E_T	threshold energy
e^-	electron
f_n	Spin-dependent coupling of a WIMP to a neutron
f_{neck}	Survival fraction of neck events
f_p	Spin-independent coupling of a WIMP to a proton
F_p	Ratio of prompt to total light in an event
F_{SD}	Spin-dependent form factor
F_{SI}	Spin-independent form factor
G_F	Fermi constant
H_2	Hydrogen
H_2O	Water

h	Planck's constant, 6.26×10^{-34}Js
J	Total nuclear spin
LR	Likelihood ratio
LR_C	Likelihood ratio calculated with P_χ and P_{GapC}
LR_B	Likelihood ratio calculated with P_χ and P_{GapB}
m_χ	WIMP mass
m_N	Mass of target nucleus
μ_N	WIMP-nucleus reduced mass
μ_n	WIMP-nucleon reduced mass
N_2	Nitrogen
N	Number of events
N_i	Charge (in PE) measured in PMT, i
ν	Photon frequency
O_2	Oxygen
$P_{\chi,i}$	Probability of measuring 1 PE in PMT i for a WIMP event
$P_{neck,i}$	Probability of measuring 1 PE in PMT i for a neck event
R	Total event rate per kg per year
R	Spherical detector radius
r	Cylindrical radius in the detector
R^*	Excited atom
R^+	Ion
R_2^*	Excited dimer
R_2^+	Ion dimer
ρ_χ	Dark matter density
ρ_0	Local dark matter density

SA	Surface area
$\langle s_n \rangle$	Expectation value of a neutrons spin within a nucleus
$\langle s_p \rangle$	Expectation value of a protons spin within a nucleus
$^1\Sigma_u^+$	Singlet state excited dimer
$^3\Sigma_u^+$	Triplet state excited dimer
σ_{WN}	WIMP-nucleus cross section
σ_0^{SD}	Spin-dependent, zero momentum transfer, WIMP-nucleus cross section
σ_{SDn}	Spin-dependent WIMP-neutron cross section
σ_{SDp}	Spin-dependent WIMP-proton cross section
σ_0^{SI}	Spin-independent, zero momentum transfer, WIMP-nucleus cross section
σ_{SI}	Spin-independent WIMP-nucleon cross section
$\langle T \rangle$	Average kinetic energy of a system
t_{exp}	Exposure time
θ	Recoil angle in the centre-of-mass frame
$\langle V \rangle$	Average potential energy of a system
v	Velocity of dark matter particle in the detector rest-frame
Z	atomic number of target nucleus
z	z coordinate in the detector

Statement of Originality

The development and testing of the likelihood ratio, and its application to alpha decays originating in the neck is my own work.

Simulations were performed using the RAT framework developed by the DEAP collaboration, in which data is generated using GEANT4. The algorithm to calculate the likelihood ratio for localized alpha particle backgrounds has been added to the RAT framework.

I have benefited from detailed discussion with colleagues at the University of Alberta as well as members of the DEAP collaboration. The design, construction and collection of data with the DEAP-3600 detector is the result of collaborative effort by all members of the DEAP collaboration.

Chapter 1

Dark Matter

1.1 Introduction

1.1.1 Evidence for dark matter

Issac Newton's law of gravitation, developed in the 17th century, has successfully predicted and explained centuries of astronomical observations [1]. For example, the gravitational force exerted by a then undiscovered planet, Neptune, accurately explained the deviation of Uranus' orbit around the Sun, as predicted by U.J. Le Verrier [2]. The discovery of Neptune by J.G. Galle in 1846 led Le Verrier to propose the existence of an additional undiscovered planet to explain the precession of Mercury's orbit. Its existence was never confirmed, and Mercury's precession was instead explained by Einstein's addition of general relativity to gravitation [3]. The law of gravitation has been further challenged in the 20th century by our understanding of the nature of matter and its distribution in the Universe. There currently exists irrefutable evidence that $\sim 26\%$ of our Universe exists as dark matter [4]. Alternative explanations to this astronomical evidence require modifications to the Law of Gravitation and general relativity [5].

Fritz Zwicky coined the term "dark matter" in an effort to explain the

discrepancy between the observed galactic rotational velocities in the galaxy cluster, Coma, and the average value calculated using the virial theorem [6]. By observing the shift in spectral lines, Zwicky calculated the rotational velocity of individual galaxies. The result was hundreds of times larger than the average value derived using individual galaxies as test particles in the virial calculation, where $\langle T \rangle = -\frac{1}{2}\langle V \rangle$. Zwicky reconciled the disagreement by proposing the existence of dark matter in quantities far greater than luminous matter [6].

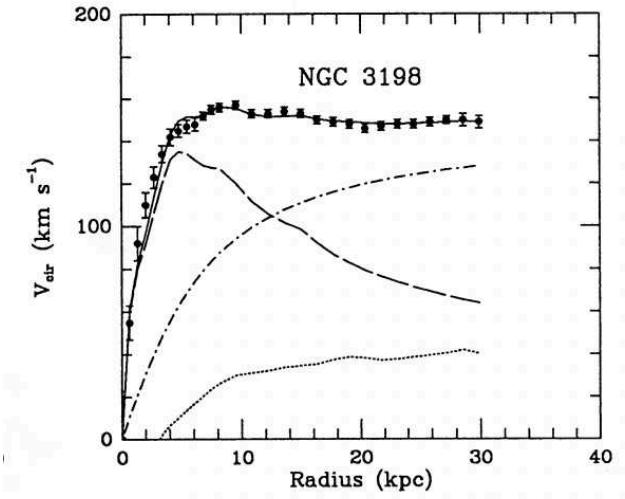

Figure 1.1: The rotation curve of NGC3198 (solid line) with three contributing elements, which include a visible component (dashed line), gaseous component (dotted line), and dark halo component (dashed/dotted line) [7].

The rotation curve of a galaxy is obtained by plotting the circular velocity of a star versus the distance from the galactic centre. From Newton's law of gravitation, the circular velocity for an orbit of radius, r, is given by $v(r) = \sqrt{\frac{GM(r)}{r}}$, where $M(r)$ is the mass inside the orbit. If the orbital radius lies outside of the visible disk of the galaxy, we expect $v(r) \propto \frac{1}{\sqrt{r}}$ [8]. Observed rotation curves, like that shown in Figure 1.1, exhibit flat behaviour that contrasts predictions made using the Law of Gravitation. The flat rotation curve can be well modelled by the inclusion of a spherical dark halo with $M(r) \propto r$ composed of non-luminous matter. Models that require modifications to the theory of grav-

itation at large radii, which do not include a dark matter component, have also been proposed to explain the anomalous flat rotation curves [9].

The effect known as gravitational lensing, where the gravitational force of a massive object bends and focuses light emitted from objects behind it, may be used to measure the distribution of matter within a galaxy cluster [10].

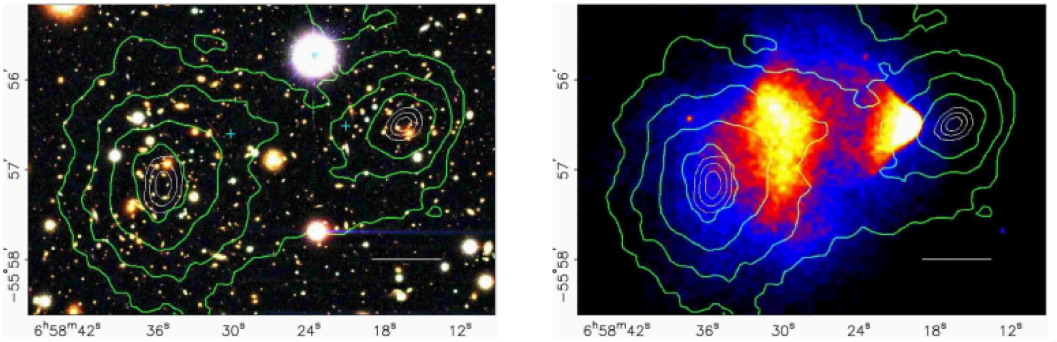

Figure 1.2: Cluster 1E 0657: Magellan image shown in the left panel, X-ray image shown in the right. The green lines in both panels show the mass distribution in the cluster measured by weak gravitational lensing [11].

In 2006, Clowe *et al* provided conclusive proof for the existence of dark matter using weak lensing observations of 1E 0657 [11]. In the merging of two galaxy clusters, as in the cluster 1E 0657, shown in Figure 1.2, the hot X-ray emitting plasma decouples from the galaxies, which behave as collisionless particles. Mapping of the mass distribution using weak lensing observations shows that the gravitational potential follows the position of the galaxies rather than the intersecting plasma which contains the dominant baryonic mass. Clowe et al not only showed that the majority of the system exists as dark matter, but also provided evidence that an alteration to the gravitational force law cannot explain the decoupling of the majority of the mass from the baryonic mass.

The study of the evolution of the Universe following the big-bang also provides evidence for the existence of dark matter. The efficiency with which the fusion of elements occurs in the early Universe is dependent on the density of baryons [10]. Immediately following the big bang, nuclei that form in the collision of protons and neutrons are instantly broken apart by high energy photons.

As the temperature cooled and the Universe expanded, the energy of photons decreased. Once the majority of photons had energies less than the binding energy of deuterium, deuterium, and other elements in turn, could be formed as they were no longer broken apart by photons [12]. This nucleosynthesis is dependent on the density of protons and neutrons and decreases as the Universe expands. Neutrons are also unstable, with a half life of about 15 minutes. Therefore, nucleosynthesis will only occur in the minutes folowing the big-bang until the neutrons are gone. By studying the amount of deuterium and other elements in primordial gas clouds, the baryon density can be determined. This results in a value of about $4.83 \pm 0.12\%$ [4], which is much less than the total matter density estimated from the mass of galaxy clusters [10, 12].

The cosmic microwave background (CMB), first detected in 1965 by radio astronomers Arno Penzias and Robert Wilkinson, depicts the conditions in the early Universe [13]. The CMB consists of relic photons that last scattered shortly after the time when matter decoupled from radiation. At this time, temperature fluctuations follow density fluctuations, and matter flows towards regions of high density and away from regions of low density. Model calculations using the density fluctuations measured from the CMB, and the baryon density determined from nucleosynthesis, do not allow for the formation of large scale structures like galaxies, clusters and superclusters. Including a non-relativistic dark matter component in these calculations enables large scale structure formation and further excludes neutrinos as dark matter candidates due to their relativistic nature [10, 12]. Analysis of the most recent CMB observations from the Planck collaboration constrain the energy density of the Universe to $69.35 \pm 0.72\%$ dark energy and $30.65 \pm 0.72\%$ matter [4]. The energy density attributed to cold dark matter can be calculated by subtracting the baryon energy density (constrained by nucleosynthesis) from the total matter energy density.

1.1.2 Dark matter candidates

Current evidence for the existence of dark matter supports a particle that is stable (or with lifetime long enough to have existed since the big-bang), interacts gravitationally, is non-relativistic (or cold) and electrically neutral. Weakly Interacting Massive Particles (WIMPs) with mass on the order of GeV/c^2 to TeV/c^2 scale and subject to weak nuclear force interactions are supported by cosmological models that match the current CMB observations [8]. No WIMP candidates exist in the current Standard Model of particle physics[5]. Studies of extensions to the Standard Model have a number of WIMP candidates as a natural result [14]. In the supersymmetric extension to the Standard Model the neutralino is the lightest stable particle and is a viable candidate for dark matter [5].

Dark matter is widely accepted as an explanation to many astrophysical observations, but its particle nature has not yet been constrained. The detection of dark matter can be categorized into three techniques: *indirect detection* seeks to observe the particles resulting from dark matter annihilation or decay; the *production* and subsequent detection of dark matter using particle accelerators; *direct detection* of the scattering of dark matter particles on terrestrial targets.

1.2 Scattering

1.2.1 Halo parameters

For the direct detection of WIMPs, the distribution of dark matter within our galaxy must be modelled. The inclusion of a spherical dark matter halo within a galaxy is strongly motivated by galactic rotation curves. This dark halo has a density, ρ_χ, that falls with r^{-2}, where r is the distance to the galactic centre. Estimates constrain the local dark matter density in the Milky Way to $0.2 \leq$

$\rho_\chi \leq 0.4$ GeV/c^{2}cm^3, which has lead to the adoption of $\rho_\chi = 0.3$ GeV/c^{2}cm^3 as in Lewin and Smith [15]. Dark matter particles are gravitationally bound to the galaxy and the simplest model assumes a Maxwellian velocity distribution [15]. This velocity distribution must be shifted to the Earth's rest frame to estimate the rate of WIMPs elastically scattering off Earth-based nuclei.

The following summary of recoil kinematics and cross sections follows the work outlined in Chapter 17 of [16] and Schnee's "Introduction to Dark Matter Experiments" [17].

1.2.2 Recoil kinematics

Direct detection experiments seek to observe the recoil signal from a WIMP with mass, m_χ, and velocity, v, elastically scattering off a target nucleus with mass, m_N. The recoil energy of such a nuclei is given by

$$E_R = \frac{\mu_N^2 v^2}{m_N}(1 - cos\theta) \tag{1.1}$$

where $\mu_N = \frac{m_\chi m_N}{m_\chi + m_N}$ is the WIMP-nucleus reduced mass, and θ is the recoil angle in the centre-of-mass frame. The most probable incident WIMP energy is $E_0 = m_\chi v_0^2/2$, and the mean recoil energy is $\langle E_R \rangle = E_0 r$, where r is a kinematic factor equal to $4m_\chi m_N/(m_\chi + m_N)^2$. This factor is always ≤ 1 and is equal to unity only in the case where $m_\chi = m_N$. For dark matter masses in the $10 - 1000$ GeV/c^2 range, and galactic velocities on the order of 10^{-3}c, typical recoil energies range from $1 - 100$ keV [15].

The differential event rate can be expressed in terms of the differential cross-section for WIMP-nucleus elastic scattering, $\frac{\mathrm{d}\sigma_{WN}}{\mathrm{d}E_R}$, and the WIMP velocity distribution in the detector reference frame, $f(v)$ (normalized to unity).

$$\frac{\mathrm{d}R}{\mathrm{d}E_R} = \frac{\rho_0}{m_N m_\chi} \int_{v_{\min}}^{\infty} v f(v) \frac{\mathrm{d}\sigma_{WN}}{\mathrm{d}E_R}(v, E_R)\mathrm{d}v \tag{1.2}$$

The lower limit of integration corresponds to the minimum WIMP speed that can cause a recoil of energy, E_R. As detectors are located within the Milky Way Galaxy, the upper limit of integration does not extend to infinity and is instead truncated at the local escape speed, v_{esc}, which is the maximum speed in the galactic rest frame at which WIMPs are gravitationally bound.

Integrating the differential event rate over all possible recoil energies, the total event rate, per kilogram, per year is given by

$$R = \int_{E_T}^{\infty} \mathrm{d}E_R \frac{\rho_0}{m_N m_\chi} \int_{v_{\min}}^{\infty} v f(v) \frac{\mathrm{d}\sigma_{WN}}{\mathrm{d}E_R}(v, E_R)\mathrm{d}v \tag{1.3}$$

where E_T is the threshold energy which corresponds to the smallest recoil energy measurable by a detector.

1.2.3 Cross sections and experimental limits

The WIMP-nucleus differential cross section is dependent on the nature of the WIMP interaction as well as the properties of the target nucleus. It can be separated into spin-independent (SI) and spin-dependent (SD) terms, which can be further decoupled into a cross section at zero momentum transfer, σ_0, and a form factor, $F(E_R)$, which contains the dependence on the momentum transfer. The WIMP-nucleus cross-section is then expressed as

$$\frac{\mathrm{d}\sigma_{WN}}{\mathrm{d}E_R} = \frac{m_N}{2\mu_N^2 v^2}\left(\sigma_0^{\mathrm{SI}} F_{\mathrm{SI}}^2(E_R) + \sigma_0^{\mathrm{SD}} F_{\mathrm{SD}}^2(E_R)\right) \tag{1.4}$$

For the spin-independent case the WIMP-nucleus cross-section is given by

$$\sigma_0^{\mathrm{SI}} = \frac{4\mu_N^2}{\pi}\left[Z f_p + (A - Z) f_n\right]^2 \tag{1.5}$$

where Z is the atomic number of the target nucleus, A is the atomic mass of the target nuclei, and $f_p(f_n)$ is the effective spin-independent coupling of a WIMP to a proton(neutron). For many models, $f_p \approx f_n$, which allows σ_0^{SI} to

be written as

$$\sigma_0^{\mathrm{SI}} \approx \frac{4\mu_N^2}{\pi} f_n^2 A^2 = \sigma_{\mathrm{SI}} \frac{\mu_N^2}{\mu_n^2} A^2 \tag{1.6}$$

where μ_n is the WIMP-nucleon reduced mass, and σ_{SI} is the WIMP-nucleon cross section. The WIMP-nucleon cross-section is a useful quantity as it is independent of the target nucleus, and it is therefore used for comparison of experimental results from detectors with different target mediums, as in Figure 1.3.

For the spin-dependent case, the WIMP-nucleus cross-section is given by

$$\sigma_0^{\mathrm{SD}} = \frac{32 G_F^2 \mu_N^2}{\pi} \frac{J+1}{J} \big(a_p \langle s_p \rangle + a_n \langle s_n \rangle\big)^2 \tag{1.7}$$

where G_F is the Fermi constant, J is the total nuclear spin, $a_p(a_n)$ is the effective spin-dependent coupling of the WIMP to the proton(neutron), and $\langle s_{p,n} \rangle = \langle N | s_{p,n} | N \rangle$ are the expectation values of proton and neutron spins within the nucleus. Experiments that are sensitive to spin-dependent WIMP interactions do not quote limits on the WIMP-nucleon cross section, but rather the WIMP-proton cross section, $\sigma_{SDp} = \frac{24 G_F^2 \mu_p^2 a_p^2}{\pi}$, and WIMP-neutron cross-section, $\sigma_{SDn} = \frac{24 G_G^2 \mu_n^2 a_n^2}{\pi}$ (with the assumption that the other interaction is negligible in each case).

1.3 Direct detection techniques

A partial list of direct detection dark matter experiments can be found in Table 1.1. Several of the experiments listed in Table 1.1 can also be found in Figure 1.3, depicting the exclusion limits of completed, upcoming and planned dark matter searches.

The scattering of a WIMP on a target nucleus can produce photons, charge and/or phonons which are collected and measured in direct detection dark mat-

ter experiments. The highest energy resolution is achievable in detectors that collect phonon signals, since $\sim$ 10 photons per keV are produced in scintillation signals, $\sim$ 100 quanta per keV in ionization signals, and $\sim$ 10000 phonons per keV in phonon signals [17]. The reduction of background signals in direct detection experiments is critical to obtain maximum WIMP sensitivity. Many experiments look at a combination of signal types for background discrimination.

Some of the basic techniques for the direct detection of WIMPs include: threshold detectors which look for nucleation bubbles resulting from energy deposition in a nuclear recoil; the collection of scintillation from nuclear recoils in a crystal or noble liquid (with or without the additional collection of the ionization signal); and cryogenic detectors which detect phonons produced by scattering events in crystals (often accompanied by the measurement of a scintillation or ionization signal) [17].

Table 1.1: List of some direct detection experiments and their properties

Experiment	Location	Signal	Target	Status
DAMA [18]	Gran Sasso	γ	NaI	running/results
SuperCDMS [19]	SNOLAB	q/ϕ	Ge/Si	planned
EDELWEISS-III [20]	Modane	qϕ	Ge	running/results
CRESST-II/III [21]	Gran Sasso	q/γ	$CaWO_4$	commissioning/running
PICASSO [22]	SNOLAB	threshold	C_4F_10	results
COUPP [23]	SNOLAB	threshold	C_3FI	results
PICO [24, 25]	SNOLAB	threshold	C_3F_8/CF_3I	running/results
NEWS [26]	SNOLAB	ϕ	Ne,He,CH_4	planned
LUX [27]	Sanford	γ/ϕ	LXe	results
XENON1T [28]	Gran Sasso	γ/ϕ	LXe	commisioning/running
PandaX-II [29]	Jin-Ping	γ/ϕ	LXe	results/running
DarkSide50 [30]	Gran Sasso	γ/ϕ	LAr	results/running
DEAP-3600	SNOLAB	γ	LAr	commisioning/running

Chapter 2 contains a detailed explanation of the fundamentals for the direct detection of WIMPs using noble liquids, and a summary of the DEAP-3600 detector. In Chapter 3, the signals originating from radioactive backgrounds

are discussed, and in particular, the background from alpha decays in the neck region of DEAP-3600 is evaluated. A likelihood ratio algorithm to reduce the background from alpha decays originating in the neck region of DEAP-3600 is discussed in Chapter 4.

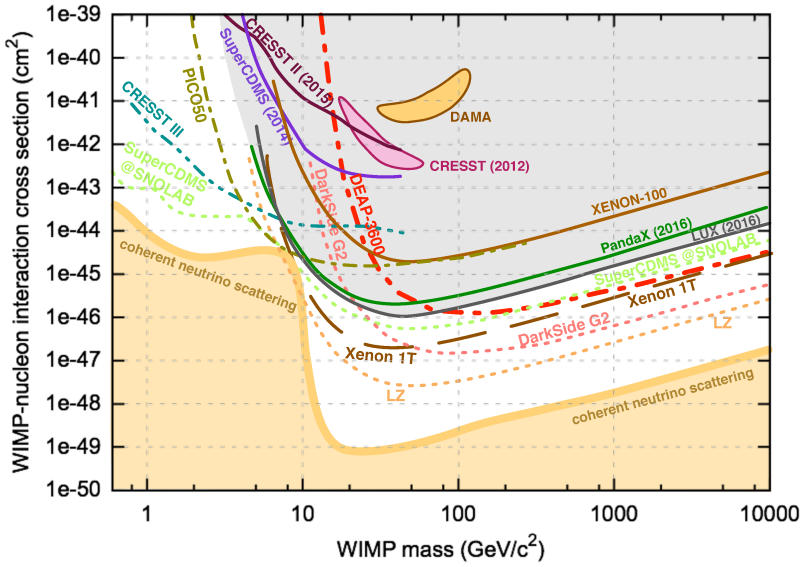

Figure 1.3: Exclusion limits for completed, upcoming and planned dark matter experiments. Solid lines correspond to completed experiments while others are dashed. The excluded region is shaded in grey while the region where neutrino scattering becomes an irreducible background is shaded orange (the neutrino scattering region is generated for a xenon target). The curves were manually digitized based on [31, 32, 29, 27]. This plot was prepared by Tina Pollmann.

Chapter 2

DEAP-3600 detecor

2.1 Noble liquids

2.1.1 Scintillation signal

Energy deposited in a noble liquid by scattering results in the ionization of atoms and eventual scintillation as the excited states decay. Experiments have shown that the scintillation wavelength is independent of the incident particle type, and the scintillation is emitted at 178 nm, 128 nm, and 78 nm for liquid xenon (LXe), liquid argon (LAr) and liquid neon (LNe), respectively [33]. In comparison to semiconductors, the scintillation properties and the relatively low cost associated with scaling detectors to large masses make noble liquids excellent target media for dark matter detection.

Incident ionizing radiation produces excited atoms, R^*, and ions, R^+, which can eventually lead to scintillation. The two possible processes are described by Eqs 2.1 and 2.2, where R is representative of any noble liquid. In Eq. 2.1 an excited atom combines with a ground state atom to form an excited dimer. In the alternative, described by Eq. 2.2, an ion undergoes a collision with a ground state atom. The resulting ion dimer recombines with an electron and undergoes de-excitation to form an excited dimer [34, 35].

$$R^* + R + R \rightarrow R_2^* + R \tag{2.1}$$
$$R_2^* \rightarrow 2R + h\nu$$

$$R^+ + R \rightarrow R_2^+ \tag{2.2}$$
$$R_2^+ + e^- \rightarrow R^{**} + R$$
$$R^{**} \rightarrow R^* + heat$$
$$R^* + R + R \rightarrow R_2^* + R$$
$$R_2^* \rightarrow 2R + h\nu$$

The emission of the vacuum-ultraviolet (VUV) photon ($h\nu$) is via the decay of an excited dimer (R_2^*) at its lowest excited level to the de-excited ground state. An important feature of the scintillation is that the photon is not energetic enough to cause further excitations in the surrounding atoms. The photon therefore propagates through the noble liquid without being absorbed. The excited dimers can exist in either a singlet, $^1\Sigma_u^+$, or triplet state, $^3\Sigma_u^+$, which have lifetimes dependent on the noble liquid, shown in Table 2.1. Excited dimers in the triplet state, $^3\Sigma_u^+$, must undergo a forbidden spin flip decay which extends its decay time in comparison to the singlet state.

2.1.2 Pulse shape discrimination

In 1977 Kubota *et al* investigated the variation in decay times for scintillation in LAr excited by electrons and alpha particles [36]. Their results did not yield a difference in decay times for the singlet and triplet states regardless of the type of ionizing radiation, but rather showed the ratio of the singlet to triplet intensities increases as a function of ionization density. This effect was opposite to that observed in organic scintillators. In noble liquids, particles

that have a higher linear energy transfer (LET), as is the case for nuclear recoils (including WIMPs), produce more singlet than triplet states. Therefore, pulse shape discrimination (PSD) can be used to identify between nuclear and electromagnetic recoils by taking a ratio of the prompt to total light measured in an interaction [37].

In addition to the dependence on LET in the ratio of singlet to triplet states, Hitachi *et al* found that the relative intensity of scintillation is also dependent on LET [33]. Less scintillation is produced by nuclear recoils than electron recoils of the same energy. This effect is known as "quenching" and L_{eff} describes the scintillation emitted by a nuclear recoil relative to an electron recoil of the same energy. Hitachi *et al* showed that the bi-excitonic mechanism, $R^* + R^* \rightarrow R + R^+ + e^-$, results in quenching and is dependent on the density of energy deposited by the radiation [38]. In this mechanism the collision of free excitons results in the production of a ground state atom, an ion and an electron, from which the ion and electron recombine to produce a photon. Assuming that each exciton would normally lead to the production of a single photon, bi-excitonic quenching causes the emission of only one photon where two photons would have been emitted if the individual excitons had not collided [39]. The biexcitonic mechanism is mostly responsible for quenching in nuclear recoils, which have high LET and therefore a higher probability of excitons colliding. Impurities in the noble liquid, such as oxygen or nitrogen, can also result in quenching over the entire range of LET. However, quenching by impurities is a more dominant effect in triplet than singlet states, and therefore strongly affects PSD [40]. It is important to limit impurities in noble liquid experiments as they will reduce the overall scintillation signal [39].

2.1.3 Choosing a detector medium

The scintillation properties of noble liquids are important to consider when selecting a medium for dark matter detection. Table 2.1 displays many of the

characteristics considered in choosing between xenon, argon and neon for dark matter detection.

Table 2.1: Scintillation wavelength, light yield, ratio of prompt to late photons (I_1/I_3), and singlet/triplet lifetimes are taken from [41]. The relative costs of xenon and neon are relative to the cost of argon, and are represented by \$.

Parameter	Xenon	Argon	Neon
Atomic number	54	18	10
Boiling point (at 1atm) [K]	165.0	87.3	27.1
Density (g/cm^3)	2.95	1.40	1.20
Cost	\$\$\$\$	\$	\$\$
Scintillation wavelength (nm)	174	128	77
Light yield (photons/keV)	42	40	15
I_1/I_3 for electron recoils	0.3	0.3	
I_1/I_3 for nuclear recoils	1.6	3	
Singlet lifetime (ns)	2.2	6	2.2
Triplet lifetime (ns)	21.0	1590	2900

As dark matter experiments using noble liquids probe smaller dark matter cross sections, the mass of detector medium must increase. Creating a uniform electric field is a known difficulty for existing dark matter detectors, and becomes more complicated as detectors transition to ton-scale target masses. Experimental designs measuring only the scintillation signal must choose between LAr and LNe as a detector medium since the difference of decay times in LXe does not provide adequate PSD for electromagnetic background reduction alone.

The light yield for nuclear recoils in LNe and LAr are shown in Table 2.1. The light yield of LAr is significantly greater than that of LNe which dominates the determination of a detectors low energy theshold. The boiling point of argon is also higher than that of neon, making the liquid state easier to achieve and more compatible with electronics in LAr than in LNe. The properties above, in addition to the lower cost of argon, make LAr the most desirable target medium to be used in a single-phase dark matter detector which only measures a scintillation signal.

The main drawback to using LAr as a detector medium is the presence of the radioactive isotope, ^{39}Ar. ^{39}Ar is a beta emitter with a half life of 269 years and an endpoint energy of 565 keV. Atmospheric argon contains ^{39}Ar with a decay rate of approximately 1 Bq/kg [42], which is produced and maintained by cosmic ray induced nuclear reactions [43]. Using Monte Carlo simulation, Boulay and Hime were the first to show that the use of PSD could reject the inherent ^{39}Ar background to a level at which dark matter detection using LAr would be competitive with LXe experiments [37]. The design of such a LAr-based detector does not require an electric field for electromagnetic background discrimination.

2.1.4 DEAP-1

The DEAP (Dark matter Experiment using Argon for Pulse shape discrimination) collaboration began its physics program with the construction of a prototype detector, DEAP-1, similar to that described in [37]. The DEAP-1 detector contained 7 kg of LAr in a cylindrical vessel viewed by 2 photomultiplier tubes (PMTs). The detector recorded data both above ground at Queen's University and 6000 metres water equivalent below ground at SNOLAB.

One of the main physics goals for the DEAP-1 detector was to show a level of PSD that would allow for sufficient background rejection in a ton-scale LAr dark matter detector [44]. The DEAP-1 analysis reported the separation of electron and nuclear recoil events using PSD for energies between 44 and 89 keV$_{ee}$ with a 6% systematic uncertainty and leakage of less than 2.7×10^{-8} for 90% nuclear recoil acceptance. A model was developed based on the DEAP-1 data that predicts a leakage of approximately 10^{-10} at 15 keV$_{ee}$ with 50% nuclear recoil acceptance for a detector with 8 PE/keV light yield [44]. This level of discrimination is sufficient to set a limit on the WIMP-nucleon cross section at 10^{-46} cm^2 for a 100 GeV/c^2 mass WIMP, a detector with a 3000 kg-yr exposure, and 8 PE/kev$_{ee}$ light yield. These specifications are the premise for the

DEAP-3600 experiment.

2.2 DEAP-3600

2.2.1 Experimental design

DEAP-3600 is a single-phase dark matter detector searching for spin-independent interactions with WIMPs [45, 46]. Argon is only sensitive to spin-independent WIMP interactions as there are no unpaired nucleons in an ^{40}Ar nucleus [17]. DEAP-3600 is located in the Cube Hall at SNOLAB with roughly 6000 metres water equivalent rock overburden. SNOLAB is located in Vale's active nickel mine in Sudbury, Ontario. The detector is designed to have 3600 kg of LAr contained within a spherical acrylic vessel (AV) that is surrounded by 255 PMTs which give roughly 76% photo-coverage of the inner volume. Maximal photo-coverage was key to the design of the detector so that the target light yield, 8 PE/keV, could be achieved. A cross section of the DEAP-3600 detector can be seen in Figure 2.1.

In a WIMP recoil event, an incoming WIMP scatters from an argon nucleus and exits the detector without further interaction. As the argon nucleus recoils, it excites surrounding atoms which form excited dimers through one of the two mechanisms described by Eqs. 2.1 and 2.2 above. Scintillation from the decay of excited dimers travels through the LAr to the inner edge of the acrylic vessel. At this point, photons are wavelength shifted from ultra-violet (128 nm) to visible wavelengths by the 3 micron coating of 1,1,4,4-tetraphenyl-1,3-butadiene (TPB). Photons are isotropically re-emitted by the TPB with an emission peak at 420 nm. The scintillation process is depicted in Figure 2.2.

The visible photons are then able to travel through the acrylic, and are directed towards the surrounding PMTs by acrylic light guides. The light guides are bonded to the acrylic vessel at one end, and are coupled to Hamamatsu R5912, 8-inch diameter, high quantum efficiency PMTs [47] at the other.

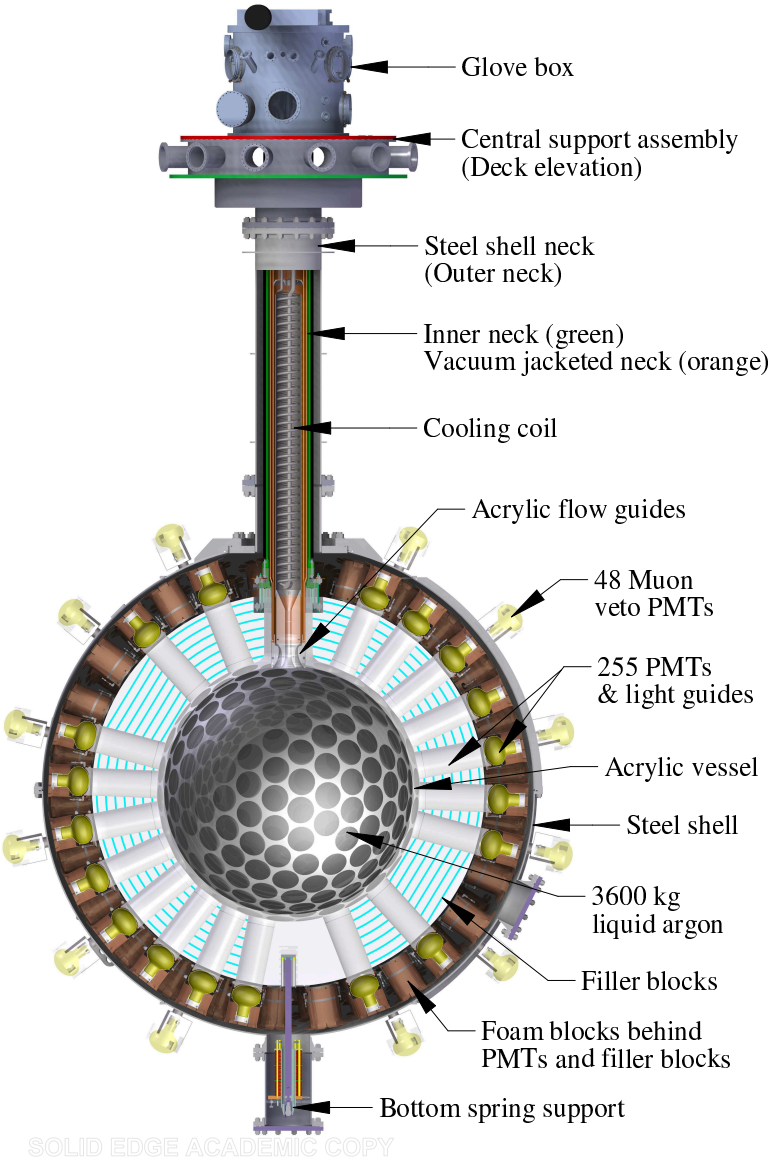

Figure 2.1: Cross section of the DEAP-3600 dark matter detector.

The signals from the PMTs are passed to custom Signal Conditioning Boards (SCBs) that shape and amplify the signal, and also send an analog sum of the signals to the Digitizer and Trigger Module (DTM), which decides when to record an event. The SCBs have both a high and low gain channel for each PMT. The output from the high gain channels are sent to CAEN V1720 digitizers and the low gain output is sent to CAEN V1740 digitizers. The low

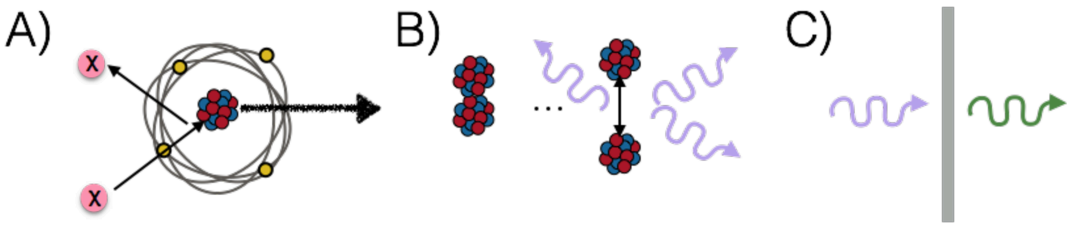

Figure 2.2: A) A WIMP scatters off an argon nucleus. The recoiling argon atom deposits energy in its surroundings. B) Excited argon dimers are formed. UV scintillation is released when the dimers decay to their ground state. C) UV photons travel to the edge of the AV where they are shifted to visible by the absorption and isotropic re-emission in the TPB coating.

gain V1740 waveform information is only collected for events which saturate the high gain V1720 channels. High gain channels are necessary to record waveforms from background events, such as alpha particles or gammas, that saturate the low gain channels. When the DTM triggers an event, the event builder extracts the signal from the digitizer and writes it to disk.

The cooling system for DEAP-3600 is based on natural convection. A steel coil filled with liquid nitrogen is installed in the neck (see Figure 2.1) to cool the LAr as it flows past. As LAr inside the acrylic vessel warms, convective currents cause the LAr to flow towards the lower neck region, shown in Figure 2.3. The detector was designed such that warm LAr moves toward the neck region where it is separated into two different flow paths established by the acrylic flow guides. The flow direction is shown with arrows in Figure 2.3. Warm LAr rises to the top of the cooling coil following the path defined by the inner and outer flow guides. After traveling ~ 3 m to the top of the neck, LAr begins flowing back towards the AV via the path containing the steel cooling coil. The LAr re-enters the AV through the opening bounded by the inner flow guide.

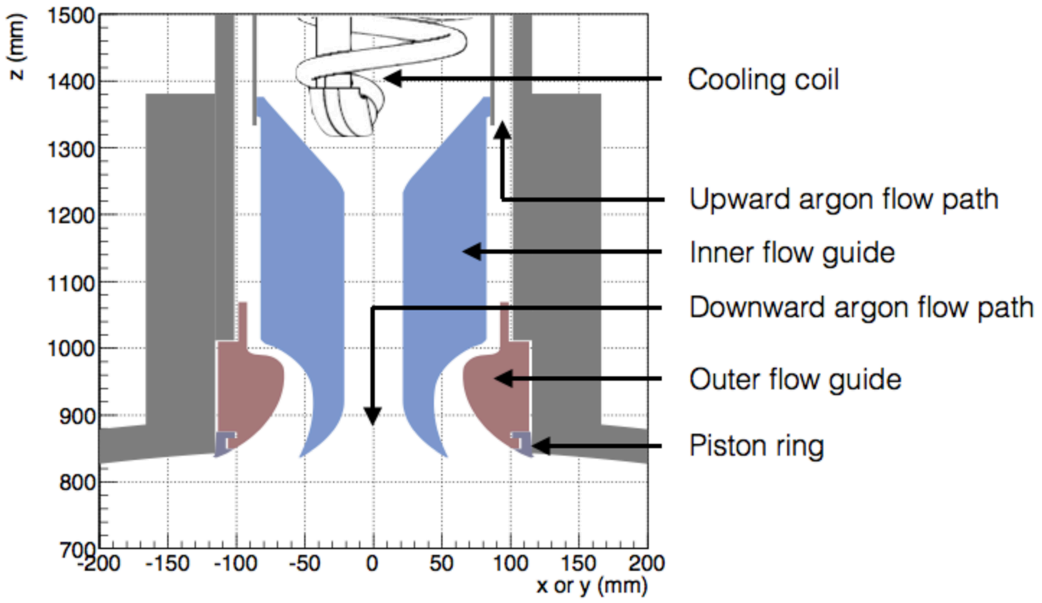

Figure 2.3: Cross section of the lower neck region containing the bolted assembly of the flow guides and piston ring. Warm LAr flows upward between the inner and outer flow guide and cool LAr flows downward through the space within the inner flow guide. Note that the scale of the dimensions between z and x/y are not equal.

The detector is enclosed in a stainless steel shell that is equipped with 48 outward facing Hamamatsu R1408 PMTs. The detector is then further submerged in a cylindrical water shielding tank that has an 8 m diameter, 8 m depth, and is filled with ultra pure water. These outward facing PMTs are part of the muon veto system used to reject through-going events which emit Cherenkov light in the water tank. At the top of the neck there is a glove box interface which allows the insertion and extraction of equipment and detector components in a low-radon environment.

2.2.2 Commisioning

The electronics for DEAP-3600 have been operational since June 2015, and commissioning data has been recorded almost continuously while completing

the construction and filling of the detector. Since June 2015 the detector has been operated with various conditions within the AV, including vacuum, nitrogen purge gas, gaseous argon (GAr) and a mix of GAr and LAr. To transition from GAr to LAr the detector had to be cooled to a temperature at which dripping LAr from the cooling coil to the bottom of the AV would not cause unsustainable thermal stresses in the AV.

From February to June of 2016 the detector underwent numerous cycles of injecting small amounts of GAr and waiting for the AV temperature to decrease and stabilize. Once the bottom AV temperature reached 120 K, the thermal stresses on the AV were small enough to permit dripping of LAr from the cooling coil into the AV. The detector started the LAr fill process on June 11, 2016 with fill speeds of $5 - 10$ kg/hr.

All data used in this work is from the first fill of the detector. All Monte Carlo simulation also assumes a full detector, corresponding to 3600 kg of LAr. The simulation will be re-evaluated once both the 3 year detector configuration has been determined and the detector optics are constrained using commissioning data.

Chapter 3

Radioactive backgrounds

The biggest challenge in probing decreasing WIMP-nucleon cross sections is the prevention and removal of signals from backgrounds in the WIMP region of interest (ROI). For DEAP-3600, these backgrounds include ^{39}Ar beta decays, neutron scatters from internal and external sources, surface alpha contamination and radon. Careful consideration during material selection and simulation of potential backgrounds were performed for DEAP-3600. Table 3.1 shows the design specifications for backgrounds in the DEAP-3600 detector [45].

Table 3.1: Background targets for DEAP-3600 [45]. Position fitter improvements will tolerate increased surface alpha activity.

Background Specification	Target
Radon in argon	< 1.4 nBq/kg
Surface α's	
with 10 cm position resolution	< 0.2 μBq/kg
with ML Fitter position resolution < 6.5 cm	< 100 μBq/kg
Neutrons (all sources, in fiducial volume)	< 2 pBq/kg
$\beta\gamma$ events, dominated by ^{39}Ar after PSD	< 2 pBq/kg
Total backgrounds	< 0.6 events in 3 tonne-years

The background targets outlined in Table 3.1 assume a detector light yield of 8 photoelectrons (PE) per keV$_{ee}$ deposited, a nuclear quenching factor, L_{eff} equal to 0.25, an analysis threshold of 15 keV$_{ee}$, and fiducial mass (radius) of 1000 kg (55 cm).

3.1 Sources of radioactive backgrounds

3.1.1 ^{232}Th and ^{238}U and their daughters

Strict material selection and protocol has been implemented in DEAP-3600 to ensure low radioactivity of detector materials. The presence of primordial ^{232}Th and ^{238}U in the vast amount of rock surrounding the detector and the diffusion of their daughter nuclei into the surrounding air is one of the main backgrounds for DEAP-3600. The decay chains of ^{232}Th and ^{238}U are shown in Figures 3.1 and 3.2 respectively. Gamma, beta, and alpha particles of varying energies are released by different daughters within the decay chains.

The daughter nuclei, ^{220}Rn and ^{222}Rn, produced in the decay chains of ^{232}Th and ^{238}U respectively, are the most troublesome isotopes due to their ability to escape the material in which the parent nucleus decays. Radon diffuses into surrounding air and is at particularly higher levels when surrounded by rock containing primordial uranium and thorium. Both radon isotopes decay to isotopes of polonium, which is ionized, allowing it to adhere to surrounding surfaces. This plate-out of radon daughters is referred to as surface contamination and is a major background concern for DEAP-3600. Figure 3.1 includes the decay chain for ^{220}Rn, which reaches a stable isotope, ^{208}Pb, within several hours 3.1. In contrast, the decay chain of ^{222}Rn, shown in Figure 3.2, contains ^{210}Pb which has a 22 year half-life. ^{210}Pb introduces a continuous source of 5.3 MeV alpha particles when the daughter nuclei, ^{210}Po, decays to the stable isotope ^{206}Pb.

The distance an alpha particle will penetrate is dependent on the material in which it is moving as well as the energy at which it is emitted. In DEAP-3600, only alpha decays occurring less than 80 microns from the LAr, in either the TPB or acrylic, are capable of producing signals that enter into the WIMP ROI [49]. Alpha decays occurring in the LAr itself have energies much higher than the ROI and can therefore be identified. Alpha particles can also cause

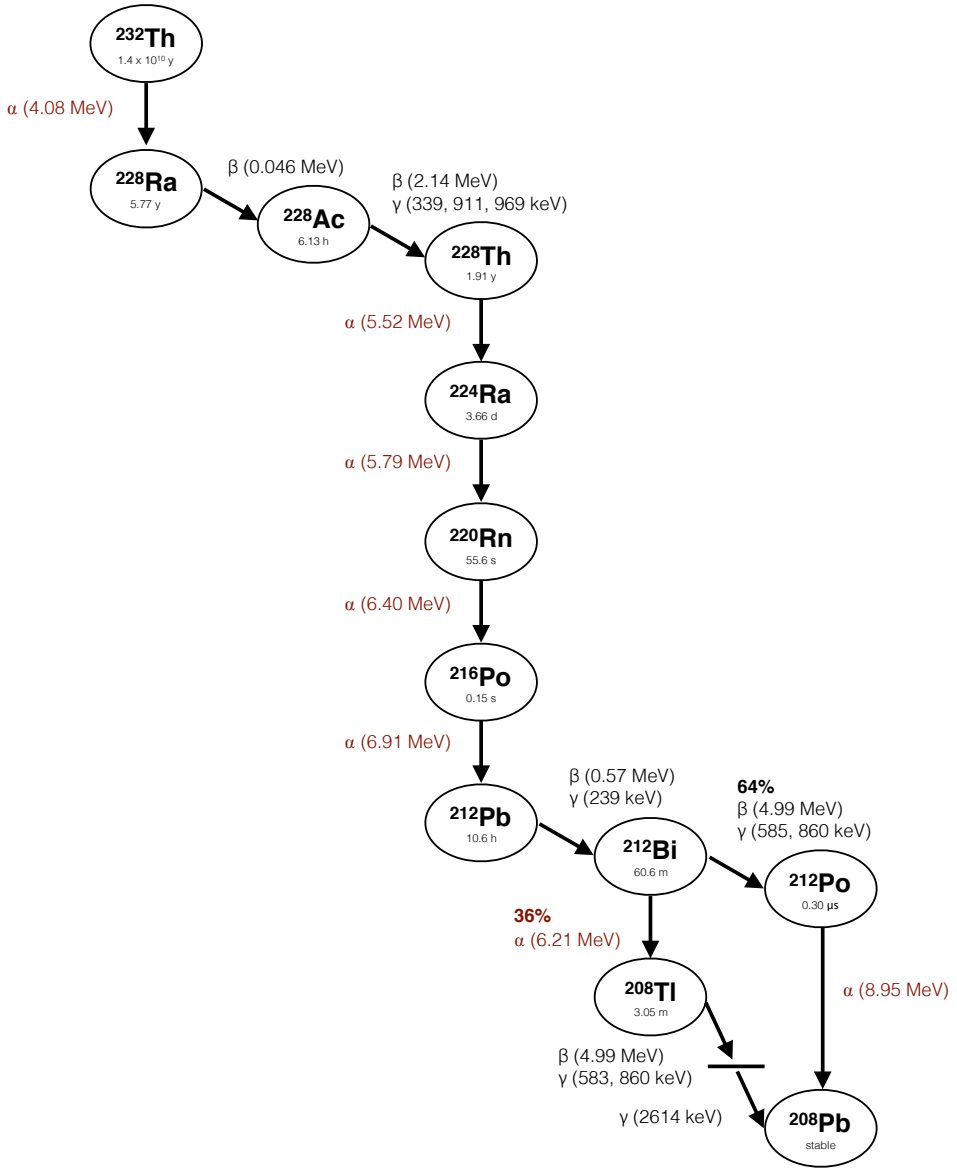

Figure 3.1: Decay chain of ^{232}Th with lifetimes, branching ratios and particle energies. Reproduced from [48].

the emission of a neutron when absorbed by certain nuclei. The neutrons from these (α,n) reactions can then enter the LAr and produce a background signal in DEAP-3600 [39]. Such reactions in the PMT glass have been simulated and are considered in the detector's neutron background specification.

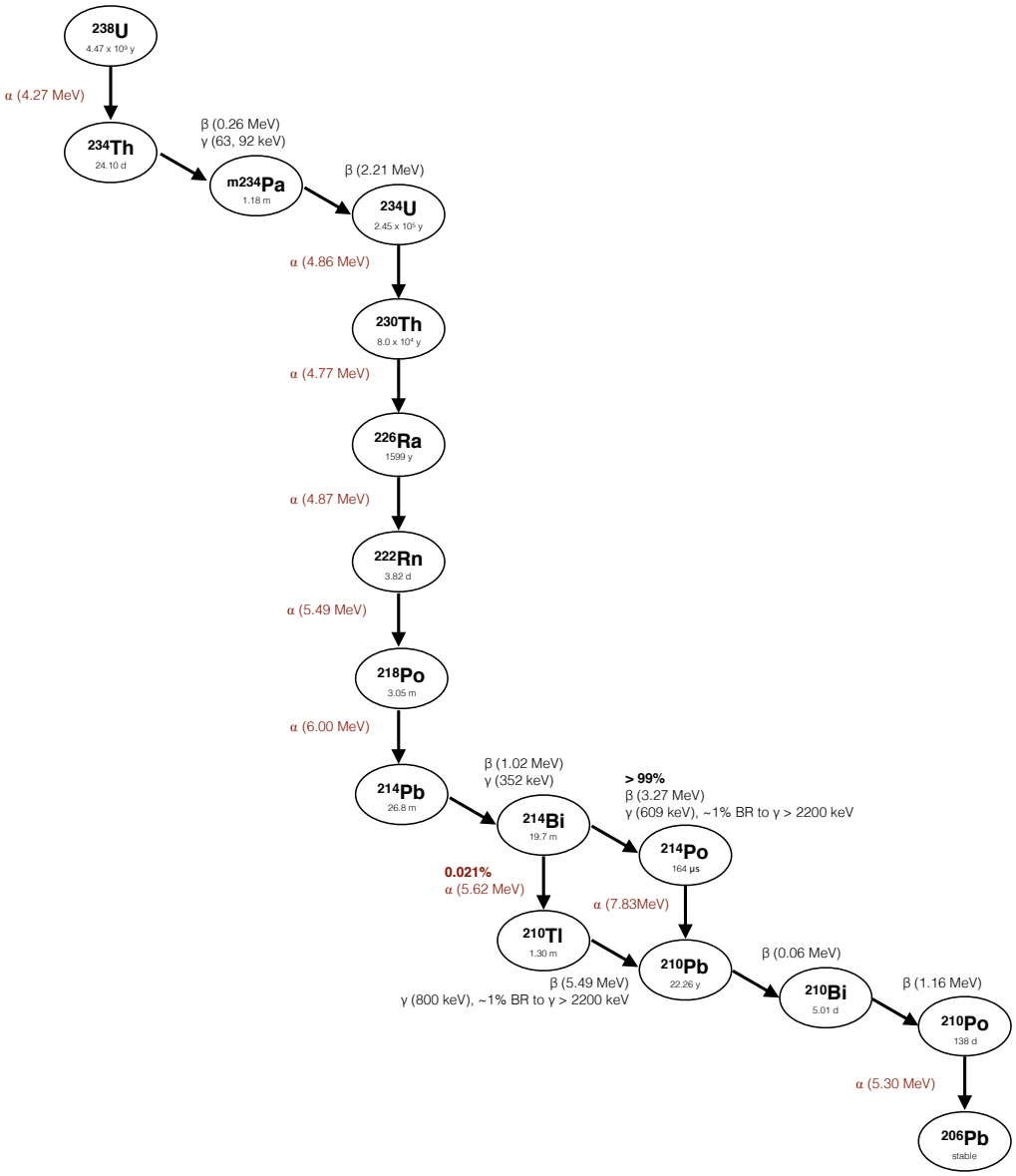

Figure 3.2: Decay chain of ^{238}U with lifetimes, branching ratios and particle energies. Reproduced from [48].

3.1.2 Cosmogenic origin

Cosmic rays, consisting of high energy protons and nuclei, enter Earth's atmosphere producing showers of secondary particles when they collide with atmospheric molecules. In DEAP-1, the cosmic ray muon flux was approximately 10 per second when operated at the surface at Queen's University. This flux decreased to roughly 1 per year when the detector was relocated to SNOLAB [44].

The 6000 meter water equivalent overburden of rock provides excellent shielding from cosmic ray muons, which, aside from neutrinos, are the only cosmic ray induced particles capable of penetrating the Earth this deeply. Neutrons induced by muon spallation in the surrounding rock must also be considered in the background specifications.

^{39}Ar is an isotope that is produced by the interaction of a cosmic ray with ^{40}Ar in the atmosphere. Therefore, LAr sourced from the atmosphere contains a natural abundance of cosmic ray induced ^{39}Ar, which is a background for argon-based dark matter detectors. A source of underground argon with decreased exposure to cosmic rays would reduce the ^{39}Ar background. Efforts have been made to secure an underground source of LAr to increase the sensitivity of DEAP-3600 in a second run phase [30].

In DEAP-3600 β decays from ^{39}Ar will be removed by PSD. As outlined in Chapter 2, DEAP-1 showed that discrimination using PSD is achievable with leakage small enough to allow DEAP-3600 to probe cross sections of approximately 10^{-46} cm^2 for a 100 GeV/c^2 mass WIMP. The designated PSD variable in DEAP-3600, F_p, is defined in Eq 3.1 as the ratio of the prompt to total charge detected by the PMTs. The nominal prompt and late time windows are [-28,150] and [-28,10000] ns, with respect to the event time. These time windows will be optimized using calibration data to achieve the largest separation between electron and nuclear recoils. Electron recoils, with more triplet than singlet dimers, are expected to have $F_p \sim 0.3$, and nuclear recoils (WIMPs) are expected to have $F_p \sim 0.7$.

$$F_p = \frac{PE_{prompt}}{PE_{total}} \tag{3.1}$$

3.2 Background reduction

In order to achieve the background specifications outlined in Table 3.1 numerous steps have been taken during the design and construction of DEAP-3600. These steps include assaying of materials for radio purity, limiting exposure of detector components to radon, passive and active shielding, and designated analysis techniques.

3.2.1 External backgrounds

To reduce the signal from high energy muons that penetrate the rock overburden, outward facing PMTs are used to veto any events which produce Cherenkov light in the water-shield. The water shield is also important for stopping gammas and neutrons produced by radioactivity and muon spallation in the surrounding rock. During commissioning, the data rate was reduced from $\sim$ 90 Hz to about 2 Hz as the water tank was filled with ultra-pure water. The event rate in an empty detector, shown in Figure 3.3, is dominated by Cherenkov light in the acrylic light guides produced by gammas originating from uranium and thorium decays in the rock wall.

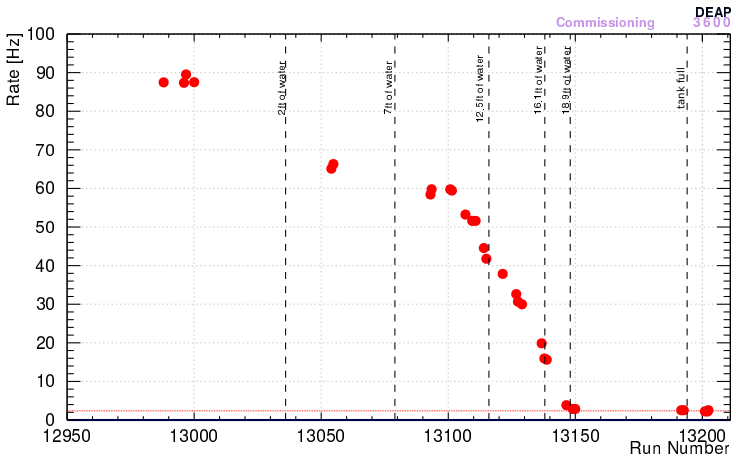

Figure 3.3: Event rate in vacuum phase of the DEAP-3600 detector as a function of water fill. The event rate in an empty detector is dominated by Cherenkov emission from gamma rays emitted by the surrounding rock wall.

3.2.2 Materials selection and design

Acrylic light guides not only provide thermal shielding between the LAr and PMTs, but also provide neutron shielding that is important to achieve the background specifications. The (α,n) reactions in the PMT glass release neutrons, with energies between $1-12$ MeV [50], which can undergo nuclear recoils if they reach the LAr. The leakage of neutrons from (α,n) reactions into the WIMP ROI increases with the energy of the neutron emitted in the PMT glass. Increasing the in acrylic path length that neutrons must travel from the PMT glass to the LAr thermalizes the neutrons, shifting their energy below the WIMP energy ROI. The length of the acrylic light guides is therefore designed to reduce the neutrons from (α,n) reactions to meet target specifications while also maintaining sufficient optical transmission of photons [50].

The LAr must be free of electronegative impurities (CH_4, CO, CO_2, H_2, H_2O, N_2 and O_2) at the sub-ppm level in order to maximize the triplet lifetime of argon scintillation. A SAES getter is used to chemically purify the argon to 99.999% and reduces contaminants to less than 1 ppb. Additionally, the LAr used for WIMP detection must be as radio-pure as possible so that polonium cannot plate-out onto the AV surface post resurfacing. The design specification for radioactivity within the LAr is less than 5μBq, and a purification loop is used to achieve this target prior to the LAr entering the vessel. A charcoal trap pre-cools argon gas from 300 K to 100 K which is then passed through a charcoal column to remove radon and radioactive impurities [46].

Perhaps the most important aspect for achieving the background specifications outlined in Table 3.1 is control of exposure to radioactivity in the materials used for construction. Since alpha particles can travel a maximum of approximately 80 microns in acrylic and TPB, the bulk and surface contamination of both materials must be restricted. During the manufacturing of the acrylic used for the AV, the primary background concern was ^{222}Rn diffusing into the materials producing long lived ^{210}Pb contamination in the

acrylic. Monte Carlo simulation showed maximum tolerable concentrations of $^{232}\text{Th} < 1.3 \times 10^{-12}$ g/g, $^{238}\text{U} < 0.3 \times 10^{-12}$ g/g and $^{210}\text{Pb} < 1.1 \times 10^{-20}$ g/g in the acrylic [51]. In these limits, secular equilibrium is assumed for ^{232}Th and ^{238}U, and the ^{210}Pb limit is 8.4 times the ^{238}U equilibrium level. The collaboration performed an assay of the acrylic used for DEAP-3600 by vapourizing a 2 kg offcut of the AV. The results constrained the ^{210}Pb contamination to less than 10^{-19} g/g [52]. The TPB deposited on the inner AV surface was also assayed and upper limits of 0.1 and 0.5 ppm were obtained for Uranium and Thorium [53], respectively. These limits are constrained by the relatively small masses of acrylic and TPB available for assay. It is expected that most activity in the TPB is derived from radon exposure.

3.2.3 Alpha backgrounds

Calculations of the deposition depth in acrylic were performed to estimate the surface contamination from exposure to ^{222}Rn and its daughters, including the long-lived daughter ^{210}Pb, during construction [54]. Figure 3.4 shows the calculated ^{210}Pb activity of the AV from radon exposure: 9 months exposure on surface, 6 months in mine air, and 1 month in radon reduced air, prior to sanding the inside of the AV. Simulations of radon daughters deposited within 80 microns of the AV surface result in 5×10^4 events/m^2/day with no fiducial volume or energy cuts applied. A robotic sander, referred to as the "resurfacer", was designed and deployed within the AV specifically to remove contamination deposited on the AV surface by exposure to radon in air. The resurfacer was operated for roughly 200 hours and removed approximately 4700 g of acrylic from the inside of the AV to meet target background requirements [46]. This leaves a residual activity of approximately 10 events/m^2/day from surface alpha particle contamination.

Radioactivity can be reintroduced to the LAr and AV surface via radon emanation in the welds of the process system. This makes energy and position

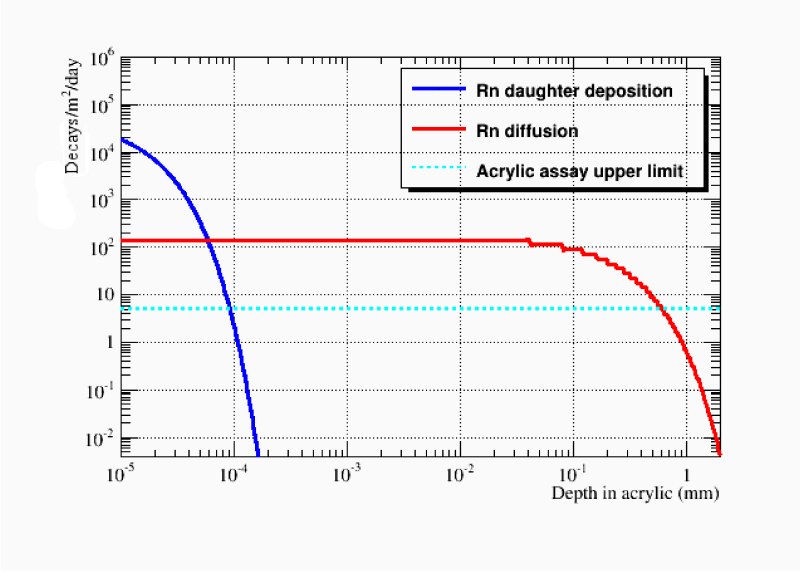

Figure 3.4: Calculated ^{210}Pb alpha particle activity as a function of depth in the AV, prior to resurfacing but after exposure to radon-laden air. The blue line shows the surface activity from radon daughter deposition, corresponding to 5 x 10^4 events/m^2/day (with no fiducial or energy cuts). The red line shows radon diffusion. The cyan line is the the acrylic assay upper limit, 2.2^{-19} g/g of ^{210}Pb in the AV [52].

reconstruction especially important for reducing alpha particle backgrounds. The observed energy of an alpha particle interaction is dependent on the location of the alpha decay. Decays occurring closer to the surface of the AV deposit a larger fraction of their energy in the LAr and can be discriminated using an energy cut. For events originating on the AV surface, surrounding PMTs observe more light, and position reconstruction algorithms use the PMT charge information to calculate the location of an event. By making a fiducial cut, discarding the outermost spherical shell of LAr where most alpha particles reconstruct (with thickness determined by the position fitter resolution) DEAP-3600 expects to meet the target alpha particle background specification.

3.3 Neck alpha particle backgrounds

3.3.1 Neck events

Alpha particles from decays in materials from the neck region are a distinct background, separate from alpha decays occurring in the AV, TPB or LAr. Alpha decays occurring in the neck region (neck events) were recognized as a possible source of backgrounds for DEAP-3600 during experimental design and subsequent investigation has been performed. Scintillation light emitted by an alpha particle interaction in the neck region is shielded from the AV by components of the neck hardware. This shielding prevents a large fraction of photons from reaching the AV. The photons that do successfully reach the AV volume must also be wavelength shifted to be detectable by the surrounding PMTs. The photon shielding causes the event energy to be underestimated, allowing events to leak into the energy ROI.

Current position reconstruction algorithms do not properly account for the complex geometry introduced by the neck hardware. The long path length for photons originating in the neck, as well as the isotropic re-emission of photons by the TPB, add to the inability to properly reconstruct the location of alpha particle interactions occurring in the neck region.

3.3.2 Preventative measures

Monte Carlo simulations of alpha particles in the neck region were used to guide modifications of the neck geometry to minimize the number of neck events in the WIMP ROI ($0.6< f_p <1$ and $120<\text{PE}<240$). An increased activity of the steel vacuum jacket, relative to the surrounding acrylic, prompted modifications to the original design to ensure no direct line-of-sight exists from the steel vacuum jacket to the AV. The shape of the inner and outer flow guides were also modified to give the smallest leakage of neck events while also maintaining the shape required for convective cooling. These modifications can be seen in

Figure 3.5. Simulations yielded particularly high neck event leakage resulting from the $\sim$ 5 mm space between the outer flow guide and the AV neck wall. This led to the design of a piston ring to prevent photons created in this small gap from reaching the AV. The piston ring has a split ring geometry which seals the space space between the outer flow guide and AV neck wall.

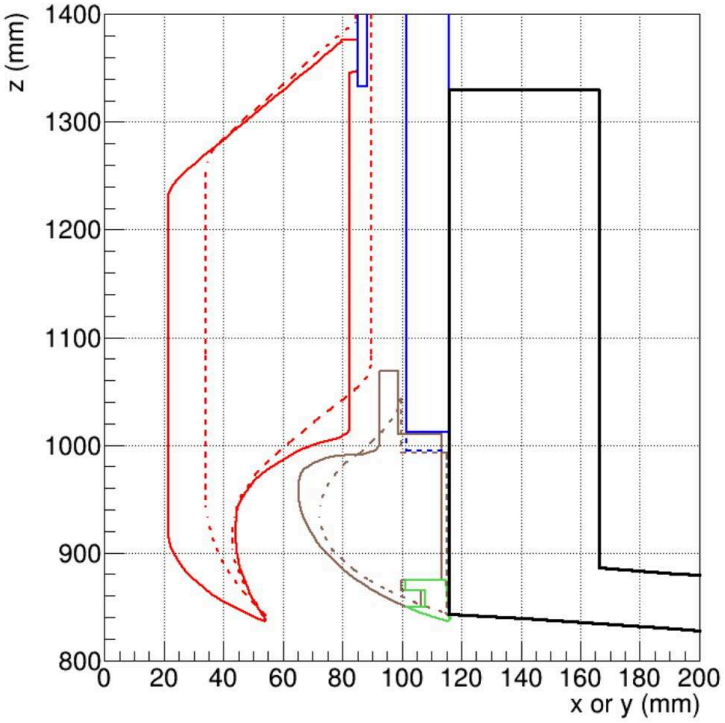

Figure 3.5: Modifications to the neck geometry based on Monte Carlo simulation studies. Dashed lines correspond to original design and solid lines correspond to the geometry which has been built. Red - inner flow guide, brown - outer flow guide, blue - steel vacuum jacket, black - AV neck wall, green - piston ring. This plot was prepared by James Bueno.

To prevent surface contamination from exposure to air, the flow guides and piston ring were machined in the low-radon clean room at the University of Alberta. An assembled view of the flow guides and piston ring at the University of Alberta can be seen in Figure 3.6. The neck hardware was sealed and shipped to Queens University where it was hand-sanded in a glove box under nitrogen purge to remove any existing surface contamination. It was then re-sealed in the canister and sent to SNOLAB where it was exposed to mine air only while

being installed.

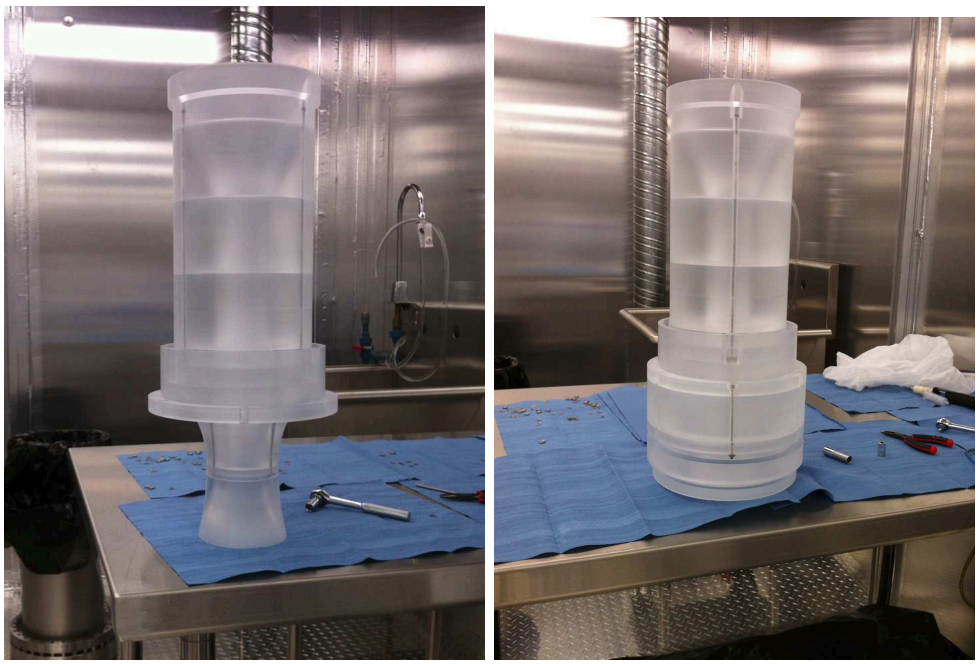

Figure 3.6: Bolted assembly of the inner (left) and outer flow guide (right) in the low-radon clean room at the University of Alberta.

A veto system is also installed in the neck of the detector, and is designed to detect optical photons created in the neck region. This neck veto system consists of wavelength shifting fibres that are bundled in groups of 50 and coupled to 4 Hamamatsu R580 PMTs. The fibres are wrapped around the bottom 10 cm of the AV neck, as seen in Figure 3.7, and the PMTs are connected to the main DAQ system [46]. Current simulations of neck events do not detect any optical photons in the neck veto. However, in commissioning data, the neck veto is triggered for a variety of event energies in the nuclear recoil f_p region. Figure 3.8 shows a sample distribution of event energy as a function of charge measured in the neck veto, with $f_p > 0.6$. Below $\sim$ 200 PE these events are dominated by cherenkov light created gammas in the neck acrylic. However, in Figure 3.8, it is clear that this distribution extends well past 200 PE and could possibly be explained by fluorescence in the neck acrylic. Acrylic fluorescence is not currently modelled in the Monte Carlo simulation, and studies are cur-

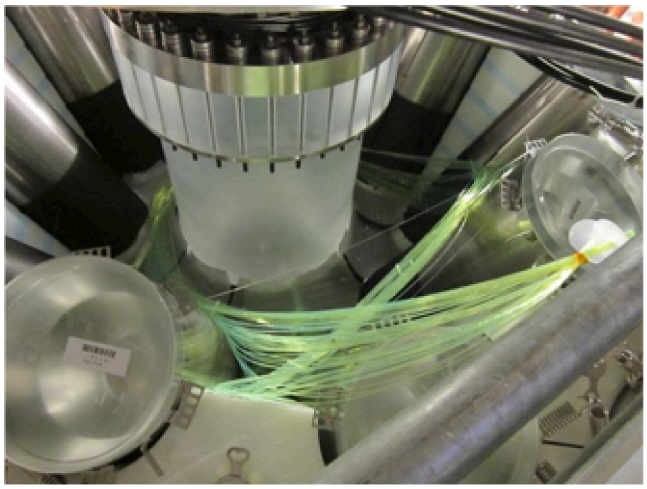

Figure 3.7: View of the neck veto fibres wrapped around the AV neck during installation.

rently being conducted to add this to the detector optics simulation. Once this is complete, simulations will be used to determine the sensitivity of the neck veto to alpha decays occurring in the neck region.

3.3.3 Monte Carlo simulation

Monte Carlo simulation of alpha decays in the neck hardware have been performed using RAT (Reactor Analysis Tool) [55]. RAT is a software framework that can generate data using GEANT4 [56], and can analyze both experimental and simulated events [46]. A custom RAT version has been developed for DEAP-3600 and has been benchmarked using DEAP-1 data. Ex-situ measurements of optical parameters have been implemented in the Monte Carlo and are important for background estimations.

Surface contamination resulting from ^{222}Rn within the LAr emits alpha particles of various energies. The energy of the emitted alpha particle can be calculated using conservation of momentum and energy. Four alpha particles are emitted in the decay chain between ^{222}Rn and ^{206}Pb with energies of 5.49 MeV, 6.00 MeV, 7.68 MeV and 5.3 MeV as shown in Figure 3.2. The observed energy spectrum and position reconstruction of alpha particles simu-

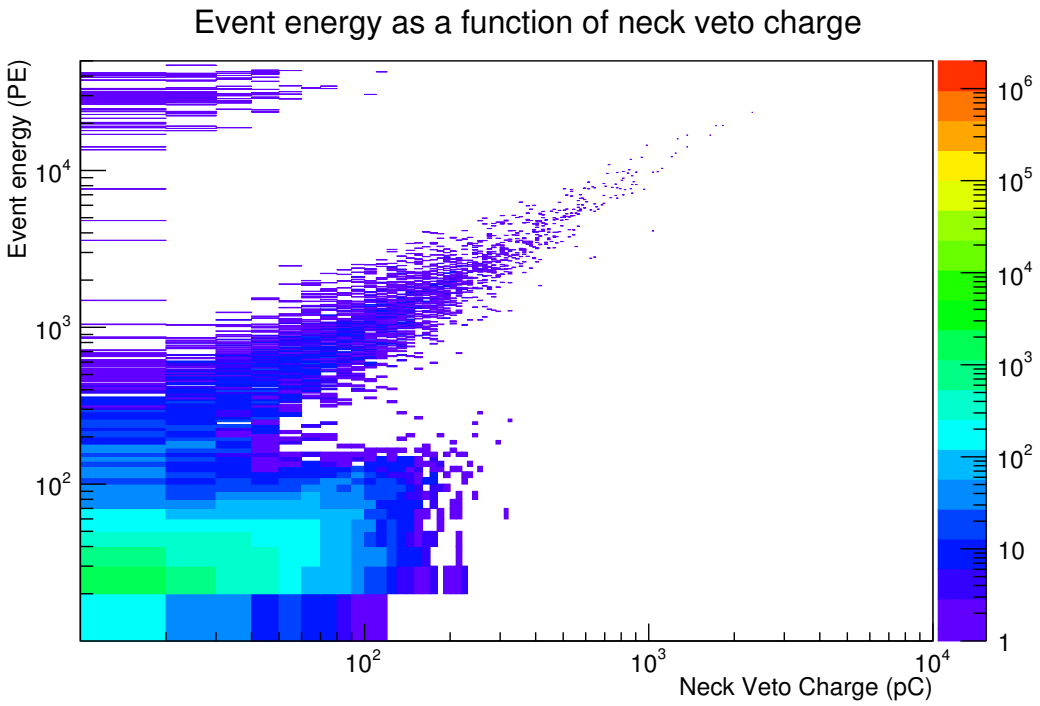

Figure 3.8: Event energy (in PE) as a function of charge measured in the neck veto (in picoCoulombs). The low energy distribution is dominated by cherenkov generated in the neck acrylic. Above 200 PE, acrylic fluorescence is likely generating visible photons that are measured in the neck veto.

lated on the surface of the inner flow guide, outer flow guide and piston ring permits the calculation of the neck event leakage into the WIMP ROI.

The observed energy distribution from the simulation of 5.3 MeV alpha particles in the neck region can be seen in Figure 3.9. Gap C corresponds to the inner edge of the inner flow guide. Gap B corresponds to the outer edge of the inner flow guide, the inner edge of the outer flow guide, and the inner edge of the piston ring. Gap A corresponds to the outer edge of the outer flow guide and the outer edge of the piston ring. The features in this distribution are a direct reflection of the line of sight from the start position of the alpha particle to the AV. Higher energies result from alpha particles that have the most direct path from the neck region into the AV, since less of the scintillation light is shadowed by neck hardware.

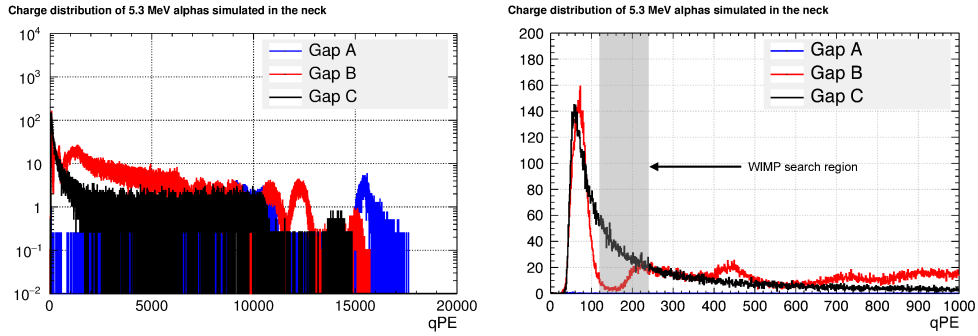

Figure 3.9: Energy distribution of 5.3 MeV alphas simulated on the surfaces of the inner flow guide, outer flow guide and piston ring. The left shows the full energy spectrum in log scale and the right shows the energy distribution from 0-1000 PE. Normalized to equal activity on each surface.

Figure 3.10 shows the origin and resulting position reconstruction of events in the WIMP ROI from surface contamination simulated on the acrylic surfaces of the neck region. Alpha particles are simulated uniformly on the surfaces of the inner flow guide, outer flow guide and piston ring, and the distributions are normalized to the number of neck events expected in 3 years, which will be discussed below. In Figure 3.10, it is clear that alpha particles originating in Gap C are those most likely to leak into the WIMP ROI. The position reconstruction of alpha particles originating in Gap B is more diffuse and reflects the more complicated path that photons travel to reach the AV. The simulations show that the leakage of events from Gap A is negligible.

3.3.4 Estimating neck event leakage

The target background for alpha particles in DEAP-3600 is < 0.6 events/3yrs, assuming an 8 PE/keV light yield and a 1000 kg fiducial mass. The contribution from neck events to the alpha particle background can be estimated using Monte Carlo simulations. The leakage of neck events into the WIMP ROI can be quantified by dividing the number of neck events that survive a series of cuts by the total number of alpha particles simulated. These cuts include: $f_p > 0.6$, $120 < \text{PE} < 240$, and a fiducial volume cut. The number of neck events is then

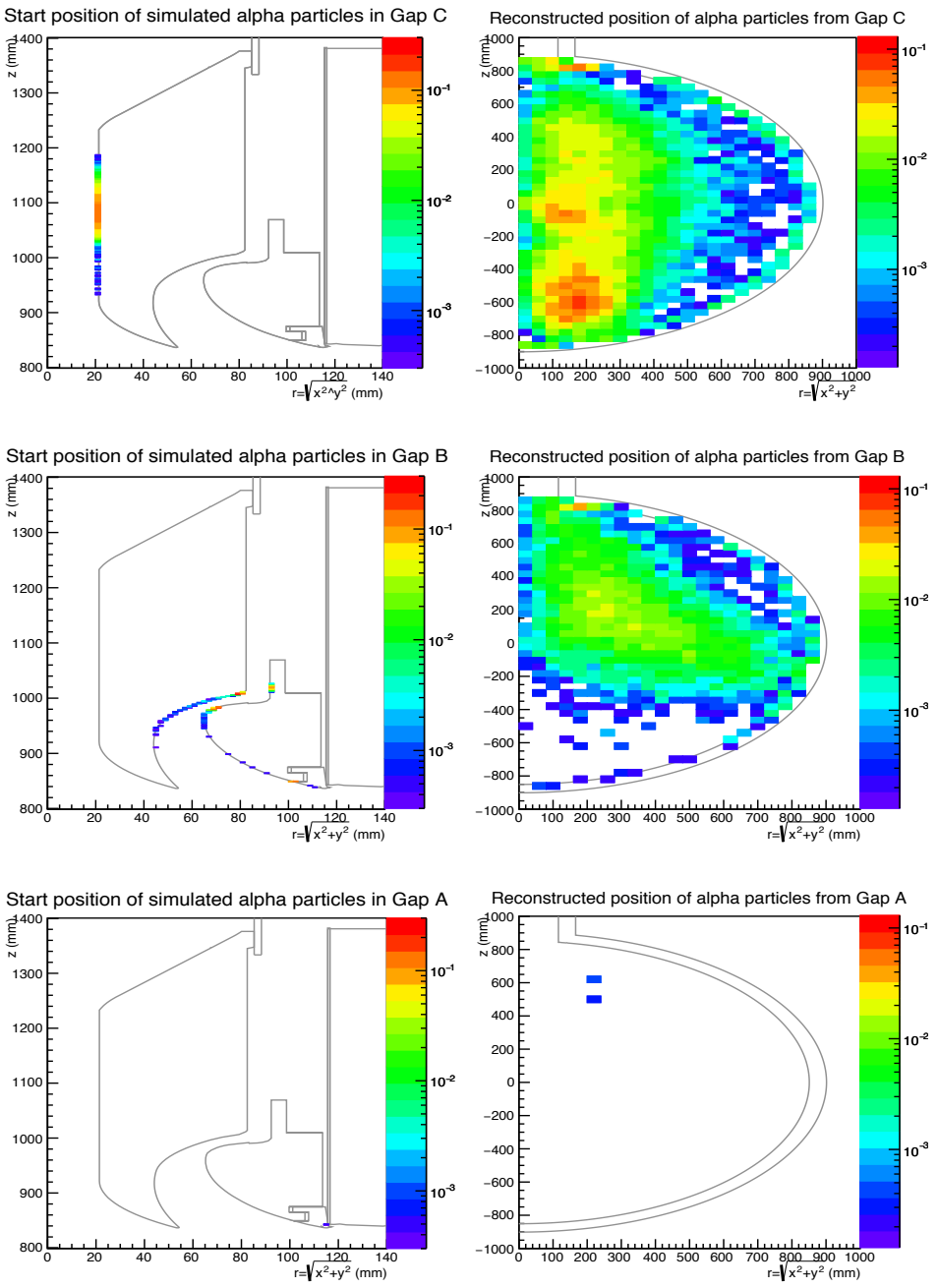

Figure 3.10: True and reconstructed position of surface contamination (^{218}Po,^{214}Po and ^{210}Po) simulated uniformly on the surfaces of the inner flow guide, outer flow guide and piston ring. Alpha particles in these distributions have $120 < \mathrm{PE} < 240$ and $f_{prompt} > 0.6$ and are normalized to the number of events in 3 years from Table 3.2.

given by

$$N = t_{exp} \times SA \times A_{surf} \times f_{neck} \tag{3.2}$$

where N is the number of events, t_{exp} is the exposure time, SA is the surface area with activity, A_{surf}, and f_{neck} is the survival fraction of neck events in the WIMP ROI.

Imposing a spherical fiducial cut, which is required for the reduction of alpha decays occurring on the AV surface or in the TPB, does not significantly reduce the number of neck events in the WIMP search region. A conical fiducial cut, which removes a section at the top of the detector in addition to the spherical region also removed, has been proposed to account for reduced resolution of position reconstruction algorithms in the neck region. The neck region is not well modelled in current position algorithms since spherical symmetry of the detector is assumed. However, significant effort is being made to implement a more realistic geometry and optical model in position reconstruction. The effect of applying a conical fiducial cut to neck events can be seen in Table 3.2.

Table 3.2 contains estimates of the number of neck events resulting from surface contamination of the neck hardware in a 3 year exposure. The source activities used in these calculations are conservative estimates, and an explanation of their derivation can be found in Appendix A. Estimates corresponding to no fiducial cut as well as both spherical and conical fiducial cuts have been calculated. A spherical fiducial cut, which removes events outside, $R = 551$ mm, corresponds to a fiducial mass of 1002 kg. The conical cut used in these studies keeps an equivalent fiducial mass as the spherical cut by increasing the radius of the remaining spherical volume to $R = 566$ mm. Neck events can be significantly reduced by imposing fiducial cuts that are motivated by simulation, however, the reduction in the number of neck events must be weighed against the loss in fiducial mass. The fiducial mass of the experiment is directly

proportional to the WIMP sensitivity, as shown in Eq. 1.3.

Table 3.2: Number of neck events in 3 years for surface alpha contamination of the flow guides and piston ring. Events are evaluated in the WIMP search region: $f_{pr} > 0.6$, $120 <$ PE < 240, with either a spherical or cylindrical fiducial cut applied.

Neck Component	Gap	No Fiducial Cut	Spherical Fiducial Cut	Conical Fiducial Cut
Inner FG, inner edge	C	6.52 ± 0.04	4.31 ± 0.03	3.77 ± 0.03
Inner FG, outer edge	B	1.89 ± 0.02	1.23 ± 0.01	0.91 ± 0.02
Outer FG, inner edge	B	1.26 ± 0.02	0.87 ± 0.01	0.72 ± 0.01
Outer FG, outer edge	A	0	0	0
Piston ring, inner edge	B	0.137 ± 0.007	0.024 ± 0.003	0.009 ± 0.002
Piston ring, outer edge	A	0	0	0
Total		9.79 ± 0.05	6.45 ± 0.04	5.55 ± 0.04

The estimate of the number of neck events expected in 3000 kg-yr exposure is not only dependent on the source activities and fiducial cut applied, but also on the optics parameters used in the Monte Carlo. Varying the acrylic scattering parameter between diffuse and specular, in combination with the acrylic surface roughness, can decrease the leakage of neck events by roughly a factor of 2. The optical parameters in the Monte Carlo are currently being tuned using calibration data, and the completion of this study will likely result in variation of the predicted leakage of neck events. A complete study of the effects of optical parameters on the leakage of neck events has not been performed, but worst case simulations, based on studies of calibration data taken before the application of TPB, have been used for the calculation of values in Table 3.2. Given the uncertainty in parameters which affect the leakage of neck events into the WIMP ROI, a likelihood ratio algorithm has been developed to further reduce the number of neck events expected in the WIMP ROI. This algorithm is discussed in Chapter 4.

Chapter 4

Likelihood ratio algorithm

As outlined in Chapter 2, DEAP-3600 is currently running in a partial fill configuration to prevent the reoccurrence of a seal failure. It is not yet clear whether the detector will remain in this configuration for its 3 year physics run, and therefore, a likelihood ratio algorithm to remove neck events from the WIMP ROI has been developed using simulations of an ideal detector containing 3600 kg of LAr. In the future, the algorithm will be re-evaluated using the confirmed configuration of gaseous and/or liquid argon.

4.1 Likelihood ratio for neck event rejection

4.1.1 Charge distribution in neck events

Motivation for the development a likelihood ratio variable to discriminate neck events from WIMP events arose with the identification of a distinct pattern in the charge distribution as a function of PMT location for alpha particles simulated in the neck region. An asymmetry for neck events can be seen in the charge distribution with respect to a PMTs z-coordinate (where the z-axis is vertically aligned with the neck of the detector). In Figure 4.1, each circle is representative of a single PMT, and the colour scale indicates the average

fraction of charge detected.

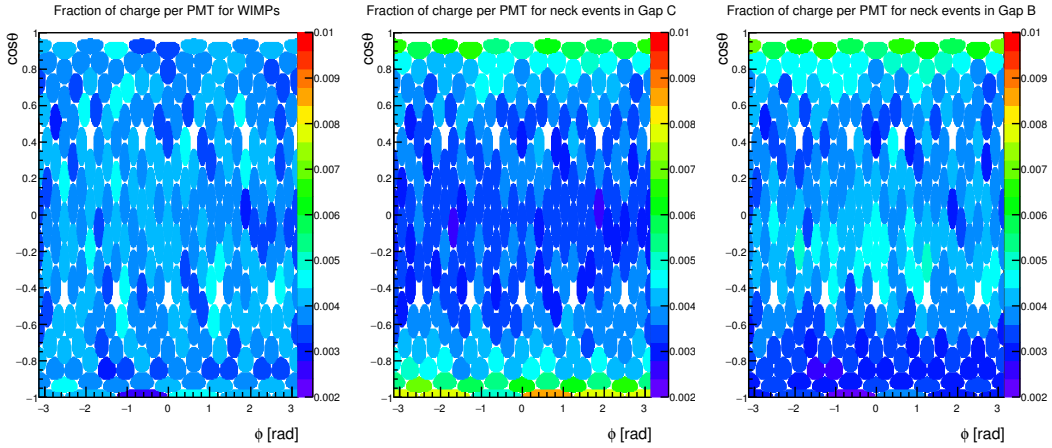

Figure 4.1: Average fraction of charge detected in an event as a function of PMT location, for events with $0 <$ PE $<$ 500. Each PMT is represented by a circle, where $cos\theta = 1$ corresponds to $z \sim 1330$ mm and $cos\theta = -1$ corresponds to $z \sim -1400$ mm. The left plot corresponds to WIMP simulations, the centre plot to neck events simulated in Gap C, and the right plot to neck events simulated in Gap B.

On average, no variation is seen in the charge distribution of neck events with respect to a PMTs ϕ coordinate — it is cylindrically symmetric. The charge distribution for alpha particles simulated in Gap C has the largest fraction of light detected in PMTs located at the bottom of the detector. Alpha particles simulated on surfaces in Gap B have a less distinct pattern, with the highest fraction of charge detected in PMTs closest to the neck region, and the lowest fraction observed in PMTs at the bottom of the detector. These distributions are a direct reflection of the solid angle between the alpha particle interaction and the AV.

4.1.2 Likelihood ratio

To utilize the information available from the variation in charge with respect to PMT(z), a likelihood ratio can be calculated. The average fraction of charge detected in each PMT as a function of PMT(z) can be converted to a probability

distribution and is used as an input in the likelihood ratio calculation. The probability distributions for alpha particles simulated in Gap C and Gap B can be seen in Figure 4.2. The probability distribution for WIMPs is flat with respect to all PMT coordinates and is represented by the shaded grey region in Figure 4.2. The red and dark blue lines in Figure 4.2 correspond to the

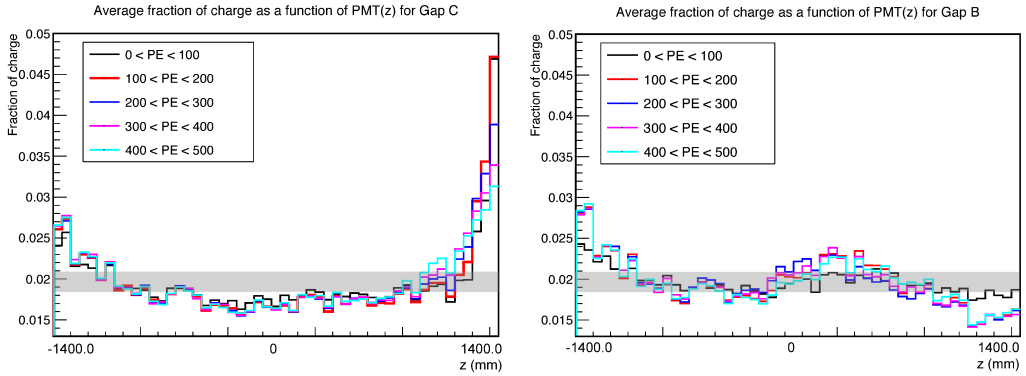

Figure 4.2: Probability distribution of the average fraction of charge detected in a PMT as a function of PMT(z). Left: alpha particles simulated in Gap C. Right: alpha particles simulated in Gap B. The shaded grey region is representative of the flat WIMP distribution. Each line is representative of events in different energy ranges.

probability distributions for events with energies in the WIMP ROI.

A likelihood ratio can be calculated to discriminate between WIMP and neck events, and is given by

$$log(LR) = \sum_{i=0}^{255} N_i(log(P_{\chi,i}) - log(P_{neck,i})) \tag{4.1}$$

where LR is the likelihood ratio test statistic, N_i is the amount of charge detected in PMT, i, and $P_{\chi,i}(P_{neck,i})$ is the probability of observing N_i in PMT i, for a WIMP(neck) event. Based on its construction, the likelihood ratio is more likely to evaluate to greater than one for WIMP events and less than one for neck events. This corresponds to a separation at zero for events in log space. LR can be used to remove neck events from the WIMP ROI by eliminating events with LR less than x. However, similar to applying a fiducial cut, a

fraction of actual WIMP events are also removed, which reduces the WIMP sensitivity of the experiment. Discrimination between neck and WIMP events is improved when two separate likelihood ratios are evaluated, LR_C and LR_B, where P_{neck} is constructed from events simulated in Gap C for LR_C and Gap B for LR_B. Outside of simulation, the origin of a neck event is unknown, and therefore LR_C and LR_B are both evaluated for all events. Using simulation, the fraction of neck events removed as a function of x for LR_C and LR_B can be calculated and is displayed in Figure 4.3. The fraction of WIMP events removed as a function of x is also displayed as the black line.

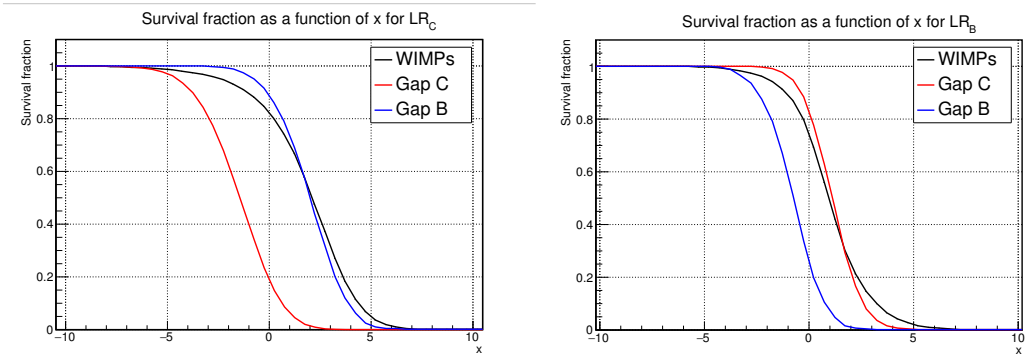

Figure 4.3: Survival fractions for LR_C (left) and LR_B (right) as a function of cut value, x. Colours are representative of the type of event simulated: WIMP events (black), neck events from Gap C (red) and Gap B (blue).

4.1.3 Likelihood ratio cut

LR_C and LR_B are not completely independent, and it is therefore important to set cut values for LR_C and LR_B based on the correlation plot of the two variables. Figure 4.4 shows this distribution for WIMP events and neck events from surface contamination simulated in Gap C and B.

To evaluate the discrimination power of a likelihood ratio cut, the neck event leakage is minimized for a likelihood ratio cut equivalent to a given fiducial mass. A fiducial mass of 1000 kg can be interpreted as a likelihood ratio cut where 28% of simulated WIMPs remain after requiring $LR_C > x$ or $LR_B > y$.

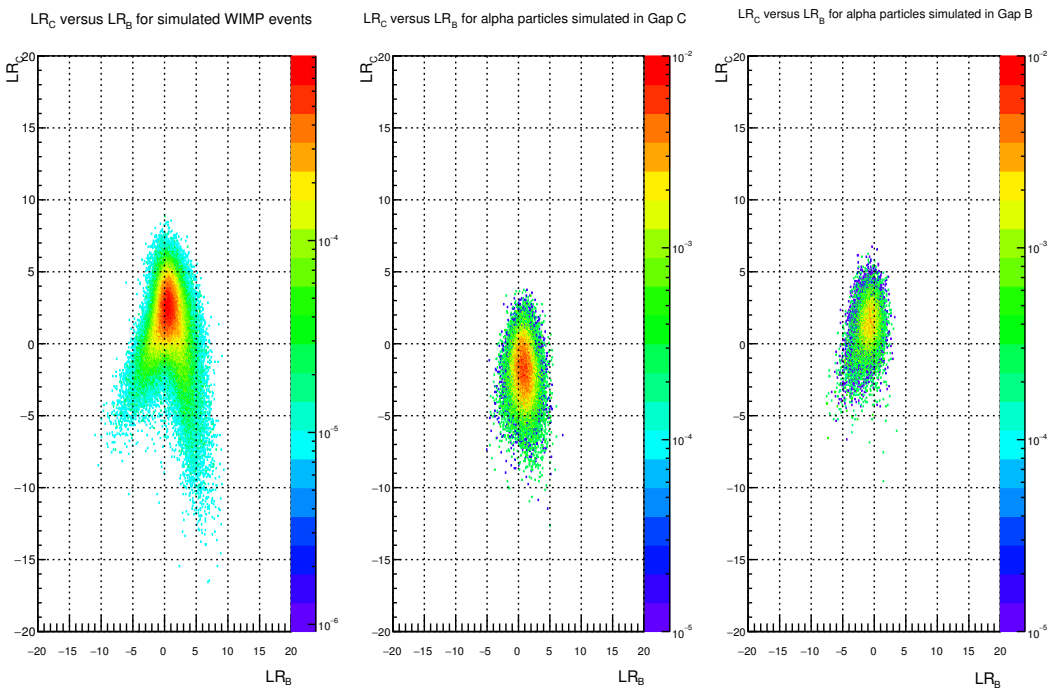

Figure 4.4: LR_C versus LR_B for WIMP events (left) and neck events simulated in Gap C (centre) and Gap B (right). The WIMP distribution is normalized to one and the neck event distributions are normalized to the estimated number of events in 3 years.

For a 28% WIMP survival fraction, the number of neck events in 3 years is minimized with $x = 1.5$, and $y = 0.8$ and can be visualized in Figure 4.5. The estimated number of neck events in the WIMP ROI, for a 3000 kg-yr exposure, corresponding to the likelihood ratio cut in Figure 4.5 can be seen in Table 4.1. The determination of x and y, based on the minimization of the number of neck events in 3 years, gives the highest statistical weight to neck events originating in Gap C since they have the highest survival fraction in the WIMP ROI.

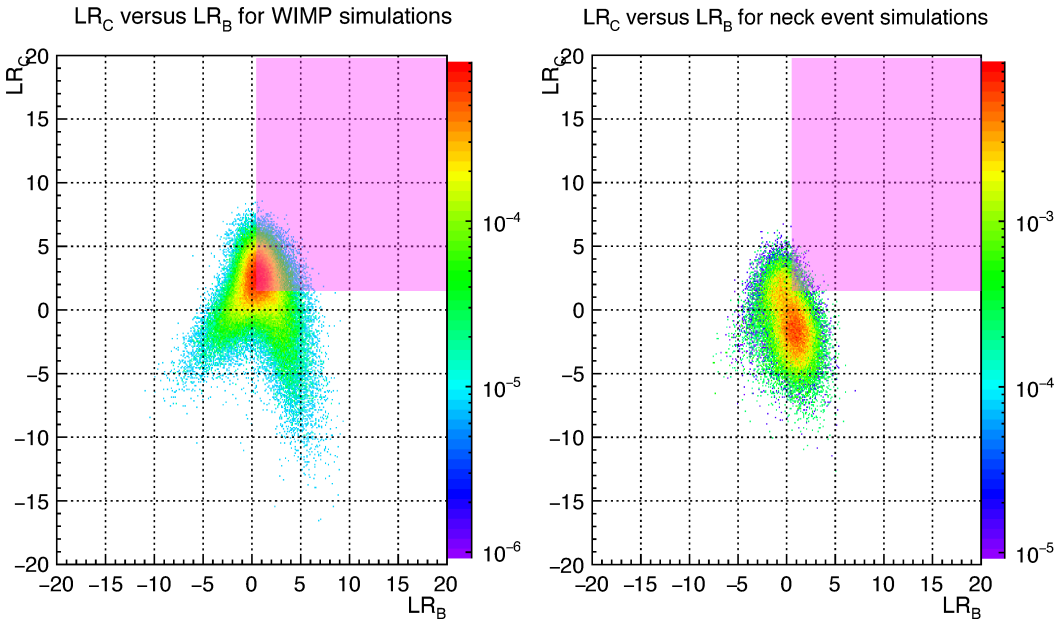

Figure 4.5: LR_C versus LR_B with events passing $LR_C > 1.5$ or $LR_B > 0.8$ in the pink shaded region. The distribution for WIMPs is shown on the left and the distribution for neck events is shown on the right. The WIMP distribution is normalized to 1 and the neck event distribution is normalized to the number of events in 3 years.

The position reconstruction of events that survive the likelihood ratio cut shows whether the likelihood ratio cut is independent of a spherical fiducial cut, and whether a pattern exists in the remaining events which could be removed with an additional fiducial cut. Figure 4.6 shows the position reconstruction of both WIMP and neck events after applying the likelihood ratio cut with $x = 1.8$ and $y = 0.5$.

Table 4.1: Estimated number of neck events in the WIMP ROI for a 3000 kg-yr exposure resulting from surface alpha contamination of the flow guides and piston ring. Events are in the WIMP search region: $f_p > 0.6$, $120 <$ PE < 240, and have either a likelihood ratio cut or combined fiducial and LR cut (respectively) applied.

Neck Component	Gap	No Cuts	LR Cut (No Fiducial Cut) $x = 1.8$, $y = 0.5$	Fiducial & LR Cut $x = 0$, $y = -2.2$, $R < 650$
Inner FG, inner edge	C	6.51 ± 0.04	0.040 ± 0.003	0.76 ± 0.01
Inner FG, outer edge	B	0.87 ± 0.02	0.048 ± 0.004	0.60 ± 0.01
Outer FG, inner edge	B	1.25 ± 0.02	0.066 ± 0.004	0.83 ± 0.01
Outer FG, outer edge	A	0	0	0
Piston ring, inner edge	B	0.137 ± 0.007	0.0002 ± 0.0002	0.0003 ± 0.0002
Piston ring, outer edge	A	0	0	0
Total		8.77 ± 0.05	0.154 ± 0.006	2.21 ± 0.02

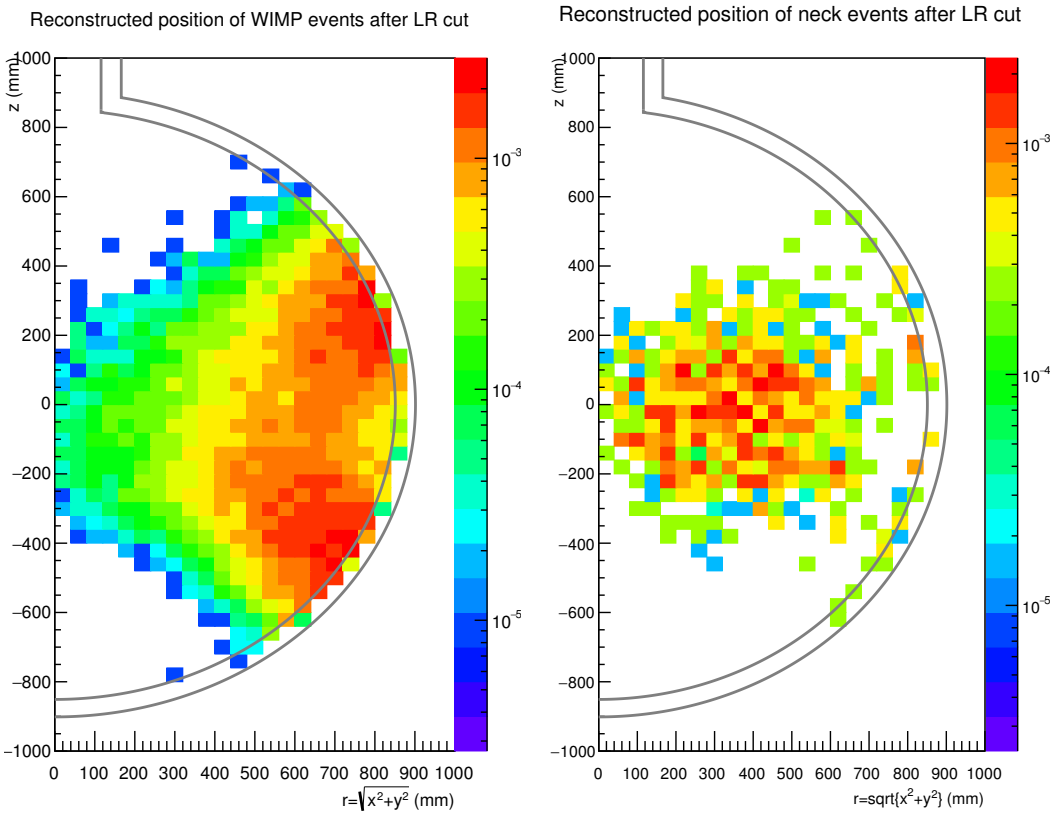

Figure 4.6: Reconstructed position of simulated WIMP events (left) and neck events (right) which pass the likelihood ratio cut, $LR_C > 1.8$ and $LR_B > 0.5$. The WIMP distribution is normalized to one prior to applying the likelihood ratio cut. The neck event distribution is normalized to the the number of neck events in a 3000 kg yr.

Despite the effective reduction in neck event leakage obtained by requiring $LR_C > 1.8$ and $LR_B > 0.5$, it is unrealistic to reduce the fiducial mass to 1000 kg with only a likelihood ratio cut since other backgrounds also impact the fiducial mass of the experiment. As discussed in Chapter 3, a spherical fiducial cut is required to remove background events from alpha decays occurring in the TPB and AV acrylic. Therefore, the reduction of fiducial mass to 1000 kg should be a combination of a spherical fiducial cut and a likelihood ratio cut. The required spherical fiducial cut will be determined by the position fitter resolution and the limits on surface activity measured in commissioning data. These studies are not yet complete, and therefore, a spherical radius of $R = 650$ mm has been evaluated in combination with a likelihood ratio cut, where $x = 0$ and $y = -1.8$, to give a combined 28% WIMP survival fraction. In this set of cuts, the spherical fiducial cut is first applied, reducing the fiducial mass to ~ 1955 kg. A likelihood ratio cut is then applied to the surviving events which results in an additional ~ 955 kg loss in fiducial mass. The number of neck events in a 3000 kg-yr exposure corresponding to the described combination of cuts is shown in Table 4.1.

Implementing a likelihood ratio cut in combination with a fiducial cut increases the neck event leakage, in comparison to solely applying a likelihood ratio cut since the majority of neck events do not reconstruct near the AV surface. However, applying the cuts in combination is a more realistic representation of a WIMP search analysis. Simulation shows that the neck event leakage is more strongly impacted by applying a likelihood ratio cut rather than a fiducial cut. It is therefore important to minimize the fiducial cut required for the reduction of other backgrounds to allow maximum neck event discrimination to be achieved with a likelihood ratio cut.

4.2 Commissioning data

4.2.1 Partial fill detector configuration

During the fill of DEAP-3600, liquid is added to the detector by dripping LAr from the cooling coil, reducing the amount of GAr in the detector as the LAr level rises. Therefore, data recorded during the first fill has a continually decreasing ratio of gaseous to liquid argon. Analysis of GAr commissioning data has shown that events from alpha decays scintillating in GAr have $f_p < 0.6$. With GAr in the neck region, neck events should be removed from the WIMP ROI by a PSD cut since the alpha particle scintillates in gas, not liquid.

In data recorded with a partially full detector, events have been observed with high energies and $f_p > 0.6$ that reconstruct near the top of the detector. These events also have charge measured in the neck veto. There is currently no understood mechanism to generate events with these characteristics, unless a thin film of LAr coats the neck hardware, which would mean an alpha particle in the neck region is scintillating in liquid rather than gaseous argon. This configuration, in combination with acrylic fluorescence discussed in Chapter 3, is currently being investigated in Monte Carlo simulation. LR_C and LR_B were developed using simulations of a full detector, containing 3600 kg LAr and should be re-tuned with new simulations once the configuration and optics of a partially full detector are better understood. However, for a partially full detector, if a thin LAr layer coats the surfaces of the neck hardware, full detector alpha particle simulations may still be representative of partial fill data since the alpha particle is scintillating in liquid rather than gaseous argon.

4.2.2 Likelihood ratio in partial fill

The effect of a likelihood ratio cut has been investigated in data recorded during the first fill of the detector. In the data shown in Figures 4.7 and 4.8, the detector contains LAr up to $z \sim 311$ mm. Figure 4.7 shows position

reconstruction and LR_C versus LR_B for events in the WIMP ROI after applying low level cuts. The distributions in Figures 4.7 and 4.8 have been normalized to unity. The class of events that reconstructs near the neck region in Figure 4.7

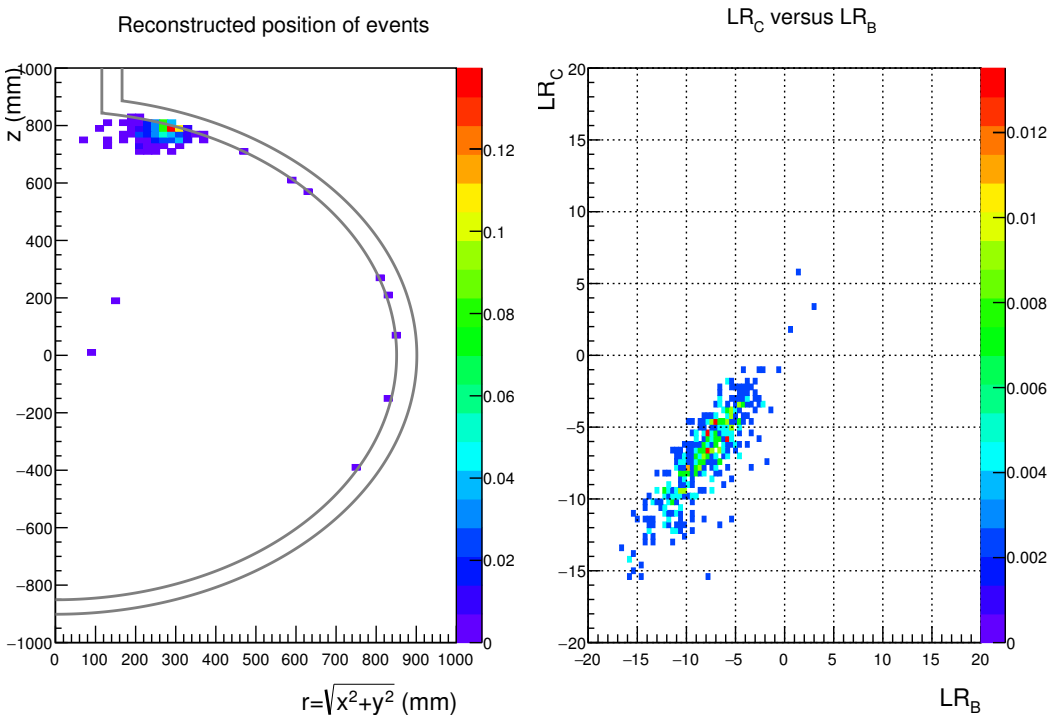

Figure 4.7: Position reconstruction (left) and LR_C versus LR_B (right) of events in the WIMP ROI recorded during the first fill of the detector, with the LAr fill level at $z \sim 311$ mm. Low level cuts have been applied.

contains events generated by cherenkov in the neck as well as an unquantified number of neck events. Biases in position reconstruction resulting from the partial fill configuration are also not fully determined and may contribute to the class of events located at near the top of the detector. In this analysis, the resulting likelihood ratio distribution is being studied.

As shown in Figure 4.7, only 2 events in this data set remain after the likelihood ratio cut, $LR_C > 1.8$ and $LR_B > 0.5$. Figure 4.8 shows the correlation between LR and the reconstructed radius or z position. The two events which pass the likelihood ratio cut reconstruct on the surface of the AV and can therefore likely be attributed to surface activity on the AV or in the TPB coating.

The events which reconstruct near the neck region are all easily excluded in the distributions of LR_C and LR_B as both variables evaluate to < 0 for all events. The survival fraction of events passing the likelihood ratio cut is equal to $0.4 \pm 0.3\%$ and is dominated by low statistics.

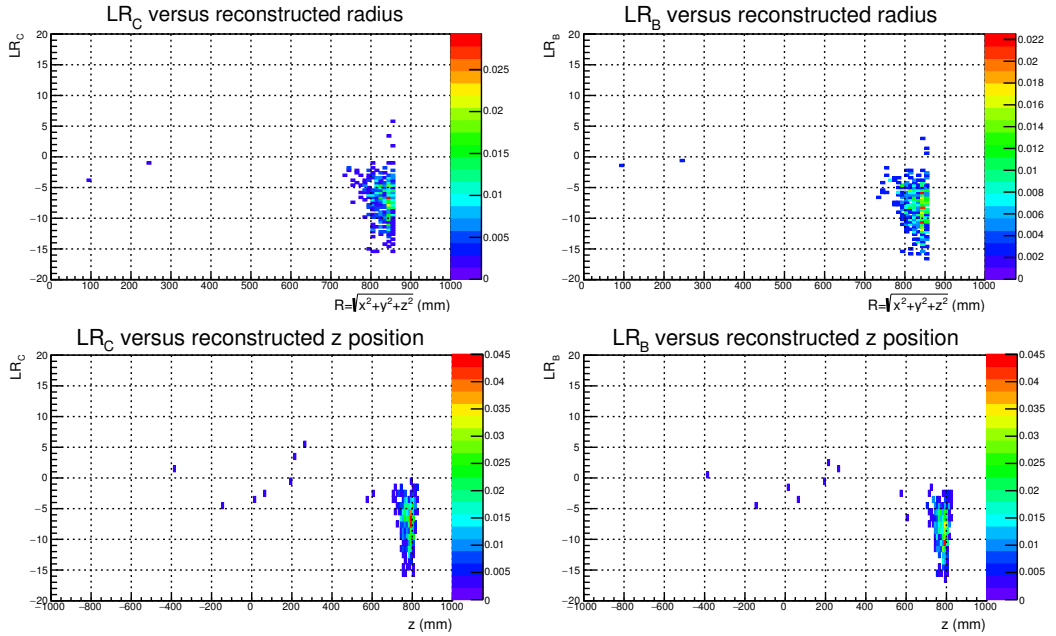

Figure 4.8: Top panel: LR_C (left) and LR_B (right) versus reconstructed radius (mm). Bottom panel: LR_C (left) and LR_B (right) versus reconstructed z position (mm). Low level and cuts to remove light guide cherenkov have been applied to these distributions.

The scintillation signal resulting from a neutron scattering on a LAr nuclei is expected to accurately model the signal from a WIMP interaction. It is therefore important to look at the distribution of LR_C and LR_B for events in the WIMP ROI with a neutron source deployed to evaluate the WIMP survival fraction of a likelihood ratio cut. Figures 4.9 and 4.10 show the same distributions as Figures 4.7 and 4.8 above, but with LAr up to $z \sim -339$ mm and an AmBe neutron source deployed at $z \sim 0$ mm. The length of time for which neutron source data was recorded is ~ 1.06 times the live-time of data considered above. Figures 4.9 and 4.10 have also been normalized to unity.

With the neutron source deployed, most events have $LR_C > 0$ and $LR_B > 0$

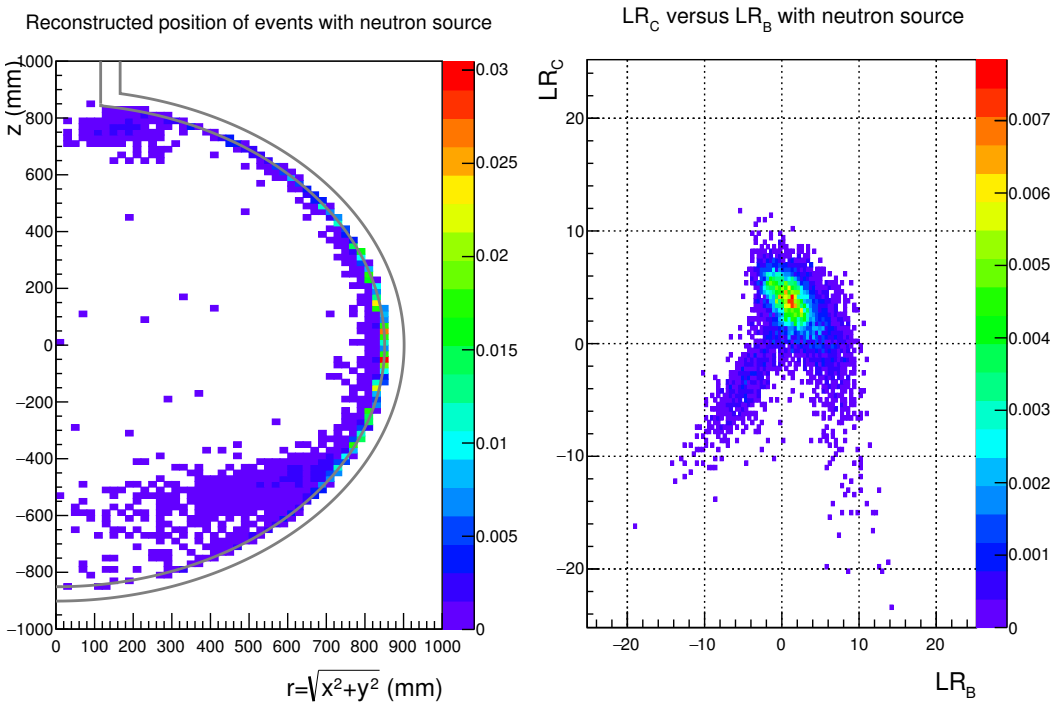

Figure 4.9: Position reconstruction (left) and LR_C versus LR_B (right) of events in the WIMP ROI recorded with an AmBe neutron source deployed in the first fill of the detector. The LAr fill level is at $z \sim -339$ mm, and low level and light guide cherenkov cuts have been applied.

which is the expected distribution for WIMP events. $40 \pm 0.8\%$ of events pass a likelihood ratio cut where $LR_C > 1.8$ and $LR_B > 0.8$. The fraction of events which pass the likelihood ratio cut and reconstruct on the AV surface can be seen in Figure 4.11. This distribution is normalized to the number of events in the WIMP ROI prior to the likelihood ratio cut. Comparing Figures 4.9 and 4.11, it is clear that a likelihood ratio cut removes events that reconstruct in a variety of locations. The likelihood ratio cut removes 100% of events which reconstruct in the neck region, as well as some events which reconstruct in the LAr and on the AV surface.

Once specific background populations have been isolated in commissioning data it will be possible to evaluate the survival fraction of different event types with respect to a likelihood ratio cut, including, but not limited to neck events.

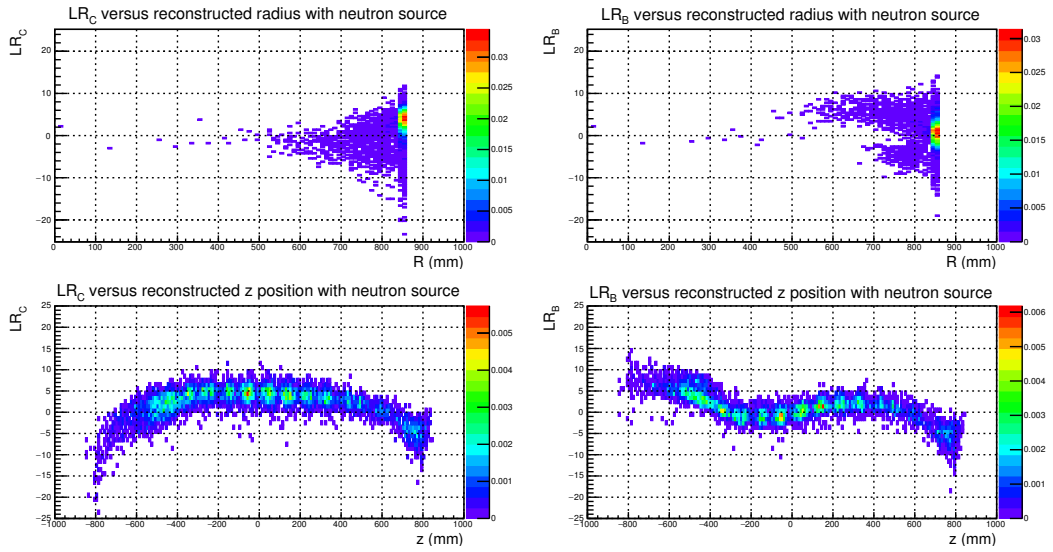

Figure 4.10: Top panel: LR_C (left) and LR_B (right) versus reconstructed radius (mm). Bottom panel: LR_C (left) and LR_B (right) versus reconstructed z position (mm). All plots have an AmBe neutron source deployed and low level cuts applied.

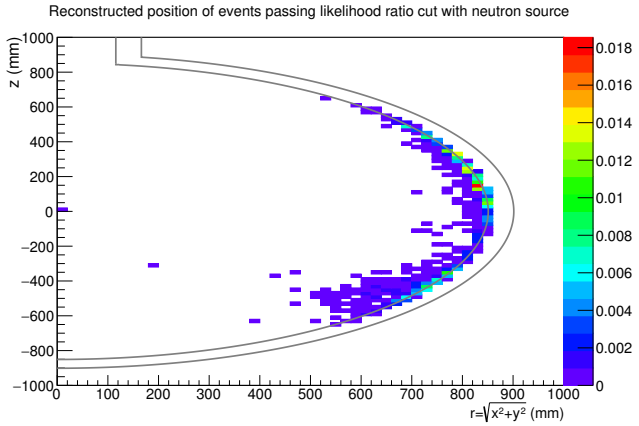

Figure 4.11: Reconstructed position of events which pass $LR_C > 1.8$ and $LR_B > 0.5$ with an AmBe neutron source deployed. Low level cuts have been applied.

The application of a likelihood ratio cut in partial fill data has removed background events that reconstruct near the neck region, where some neck events are expected to reconstruct. In addition, partial fill AmBe source data results in values of LR_C and LR_B in the WIMP ROI, showing agreement between data and simulation.

4.3 Conclusion

Alpha decays occurring in the neck region of the DEAP-3600 detector are a background concern and can impact the WIMP sensitivity of the experiment. When an alpha particle interacts in the neck region, the neck hardware prevents most scintillation from reaching the AV. This causes the energy of the alpha particle event to be underestimated and results in an event with energy and f_p in the WIMP ROI. Position reconstruction of these neck events is also poor due to the complex photon path prior to wavelength shifting and the isotropic photon re-emission by the TPB. The number of neck events expected in the WIMP ROI can be estimated using Monte Carlo simulation. This estimate is highly dependent on the optical properties implemented in the simulation, and is also impacted by the fiducial cut imposed.

This analysis shows that, in simulation, an analysis cut based on the two likelihood ratio statistics, LR_C and LR_B can be effectively used to reduce the number of neck events in the WIMP ROI for a 3000 kg-yr exposure of DEAP-3600. The likelihood ratio cut utilizes the asymmetry observed in the charge distribution of neck events with respect to a PMTs z-coordinate. Implementing a likelihood ratio cut reduces the leakage of neck events into the WIMP ROI more effectively than a fiducial cut, however, the efficiency is highly correlated with the number of WIMP events also removed by such a cut.

In simulation, applying a likelihood ratio cut which keeps 28% of WIMP events, corresponding to a 1000 kg fiducial mass, reduces the number of neck events in the WIMP ROI from an estimated 5.55 ± 0.04 events in 3 years (corresponding to a conical fiducial cut) to 0.154 ± 0.006 events in 3 years (without a fiducial cut applied). The most realistic estimate of the number of neck events in the WIMP ROI in 3 years is obtained by evaluating a likelihood ratio cut in combination with a spherical fiducial cut. Implementing a spherical fiducial cut, with $R = 650$ mm, followed by a likelihood ratio cut, where the

total remaining fiducial mass is 1000 kg, reduces the estimated number of neck events expected in a 3 year exposure to 2.21 ± 0.02.

A likelihood ratio cut is the most effective tool for removing neck events from the WIMP ROI in simulations of the DEAP-3600 detector. Simulations of neck events are currently done with parameters which cause the highest leakage of neck events, and tuning of the optical parameters based on commissioning data is expected to reduce the number of neck events expected in the WIMP ROI. Events which have light observed in the neck veto have been recorded in commissioning data, and were not expected based on the current optical model used for simulation. Implementing acrylic fluorescence in simulation will allow an estimate of the number of neck events that can be removed from the WIMP ROI by tagging of events which have light detected in the neck veto.

Additionally, the number of neck events expected in the WIMP ROI is highly dependent on the fill configuration of the detector. Alpha particles scintillating in GAr have f_p outside the WIMP ROI. If the detector remains in the current partial fill configuration, it is possible that neck events may not be a background concern. However, commissioning data has shown that the partial fill configuration results in an optically complicated detector, and further studies must be performed to understand the optics and resulting backgrounds of such a gaseous and liquid argon mixture. The application of a likelihood ratio cut to partial fill data is capable of effectively removing all events that reconstruct near the neck region. In partial fill data with an AmBe neutron source present, LR_C and LR_B have distributions representative of what is expected for a WIMP signal, and are only partially removed by a likelihood ratio cut that is motivated by simulation for the reduction of neck events. Further understanding of the classes of events present in partial fill data will permit the calculation of neck event leakage corresponding to both a fiducial and likelihood ratio cut.

Bibliography

[1] I. Newton. *Philosophiae Naturalis Principia Mathematica*. Jussu Societatis Regiæ ac Typis Josephi Streater. Prostat apud plures Bibliopolas, 1687.

[2] J. G. Galle. Account of the Discovery of the Planet of LE VERRIER at Berlin. *Monthly Notices of the Royal Astronomical Society*, 7(9):153, 1846.

[3] Thomas Levenson. *The Hunt for Vulcan and How Albert Einstein Destroyed a Planet, Discovered Relativity, and Deciphered the Universe*. Random House, 2015.

[4] P.A.R. Ade *et al.* (Planck Collaboration). Planck 2015 results xiii. Cosmological parameters. *Astronomy and Astrophysics*, 594(A13), 2016.

[5] G. Bertone, D. Hooper, and J. Silk. Particle Dark Matter: Evidence, Candidates and Constraints. *Physics Reports*, 405:279–390, 2005.

[6] F. Zwicky. Die Rotverschiebung von extragalaktischen Nebeln. *Helvetica Physica Acta*, 6:110–127, 1933.

[7] K.G. Begeman, A.H. Broeils, and R.H. Sanders. Extended rotation curves of spiral galaxies - dark haloes and modified dynamics. *Monthly Notices of the Royal Astronomical Society*, 249:523–537, 1991.

[8] J. Beringer *et al.* (Particle Data Group). Review of Particle Physics. *Physical Review D*, 86(010001):289–296, 2012.

[9] M. Milgrom. A modification of the Newtonian dynamics as a possible alternative to the hidden mass hypothesis. *Astrophysical Journal*, 270: 365–370, 1982.

[10] J. Einasto. Dark Matter. *Astronomy and Astrophysics 2010*, 2010.

[11] D. Clowe *et al.* A Direct Empirical Proof of the Existence of Dark Matter. *The Astrophysical Journal Letters*, 648(2):109–113, 2006.

[12] Barbara Ryden. *Introduction to Cosmology.* Addison Wesley, 2003.

[13] A.A. Penzias and R. W. Wilson. A Measurement of Excess Antenna Temperature at 4080 Mc/s. *Astrophysical Journal*, 142:419–421, 1965.

[14] L. Bergstrom. Non-baryonic dark matter: observational evidence and detection methods. *Reports on Progress in Physics*, 63(5), 2000.

[15] J.D Lewin and P.F Smith. Review of mathematics, numerical factors and corrections for dark matter experiments based on elastic nuclear recoil. *Astroparticle Physics*, 6:87–112, 1996.

[16] David G. Cerdeno and Anne M. Green. *Particle Dark Matter: Observations, Models and Searches*, chapter Direct detection of WIMPs. Cambridge University Press, 2010.

[17] R.W. Schnee. Introduction to dark matter experiments. *arXiv:1101.5205*, 2011.

[18] R. Bernabei *et al.* Final model independent result of DAMA/LIBRA-phase 1. *European Physical Journal C*, 73(12):2649, 2013.

[19] R. Agnese *et al.* (SuperCDMS Collaboration). Projected Sensitivity of the SuperCDMS SNOLAB experiment. *Submitted to Physical Review D*, 2016.

[20] R. Armengaud *et al.* (EDELWEISS Collaboration). Constraints on low-mass WIMPs from the EDELWEISS-III dark matter search. *Journal of Cosmology and Astroparticle Physics*, 2016, 2016.

[21] G. Angloher *et al.* (CRESST Collaboration). Results on light dark matter particles with a low-threshold CRESST-II detector. *European Physical Journal C*, 76(1):25, 2016.

[22] S. Archambault *et al.* Dark matter spin-dependent limits for WIMP interaction on 19-F by PICASSO. *Physics Letters B*, 682:185–192, 2009.

[23] W.J. Bolte *et al.* A bubble chamber for dark matter detection (the COUPP project status). *Journal of Physics: Conference Series*, 39:126–128, 2006.

[24] C. Amole *et al.* (PICO Collaboration). Dark matter search results from the PICO-2L C3F8 Bubble Chamber. *Physical Review Letters*, 114, 2015.

[25] C. Amole *et al.* (PICO Collaboration). Dark matter search results from the PICO-60 CF3I bubble chamber. *Physical Review D*, 93, 2016.

[26] S. Profumo. GeV dark matter searches with the NEWS detector. *Physical Review D*, 93, 2016.

[27] D.S. Akerib *et al* (LUX Collaboration). Results from a search for dark matter in the complete LUX exposure. *arXiv:1608.07648v2*, 2016.

[28] Aprile *et al.* (XENON1T collaboration). The XENON1T Dark Matter Search Experiment. *arXiv:1206.6288*, 2012.

[29] A. Tan *et al.* (PandaX-II Collaboration). Dark Matter Results from First 98.7-day Data of PandaX-II Experiment. *Physical Review Letters*, 117, 2016.

[30] P. Agnes *et al.* (DarkSide Collaboration). Results from the first use of low radioactivity argon in a dark matter search. *Physical Review D*, 93, 2016.

[31] P. Cushman *et al.* Snowmass CF1 Summary: WIMP Dark Matter Direct Detection. *arXiv:1310.8327v2*, 2013.

[32] G. Angloher *et al.* (CRESST Collaboration). Probing low WIMP masses with the next generation of CRESST detectors. *arXiv:1503.08065v1*, 2015.

[33] A Hitachi, T. Takahashi, N. Funayama, K. Masuda, J. Kikuchi, and T. Doke. Effect of ionization density on the time dependence of luminescence from liquid argon and xenon. *Physical Review B*, 27(9):5279–5285, 1983.

[34] T. Doke, A. Hitachi, J. Kikuchi, K. Masuda, H. Okada, and E. Shibamura. Absolute Scintillation Yields in Liquid Argon and Xenon for Various Particles. *Japan Journal of Applied Physics*, 41:1538–1545, 2002.

[35] Elena Aprile and Laura Baudis. *Particle Dark Matter: Observations, Models and Searches*, chapter Liquid noble gases. Cambridge University Press, 2010.

[36] S. Kubota, M. Hishida, and A. Nohara. Variation of scintillation decay in liquid argon excited by electrons and alpha particles. *Nuclear Instrunments and Methods*, 150(3):561–564, 1978.

[37] M.G Boulay and A. Hime. Technique for direct detection of weakly interacting massive particles using scintillation time discrimination in liquid argon. *Astroparticle Physics*, 25(3):179–182, 2006.

[38] A. Hitachi, T. Doke, and A. Mozumder. Luminescence quenching in liquid argon under charged-particle impact: Relative scintillation yield at different linear energy transfers. *Physical Review B*, 46(18):11463–11471, 1992.

[39] T. Pollman. *Alpha backgrounds in the DEAP dark matter search experiment.* PhD Thesis, Queen's University, August 2012.

[40] S. Kubota, M. Hishida, M. Suzuki, and J. Ruan. Liquid and solid argon, krypton and xenon scintillators. *Nuclear Instruments and Methods*, 196: 101–105, 1982.

[41] M.G Boulay and A. Hime. Direct WIMP detection using scintillation time discrimination in liquid argon. *arXiv:0411358v1*, 2004.

[42] P. Benetti *et al.* Measurement of the specific activity of ^{39}Ar in natural argon. *Nuclear Instuments and Methods in Physics Research A: Accelerators, Spectrometers, Detectors and Associated Equipment*, 574(1):83–88, 2007.

[43] Xu *et al.* A study of the trace ^{39}Ar content in argon from deep underground sources. *Astroparticle Physics*, 66:53–60, 2015.

[44] P.-A. Amaudruz *et al.* Measurement of the scintillation time spectra and pulse-shape discrimination of low-energy β and nuclear recoils in liquid argon with DEAP-1. *Astroparticle Physics*, 85:1–23, 2016.

[45] P.-A. Amaudruz *et al.* (DEAP-3600 Collaboration). DEAP-3600 Dark Matter Search. *Nuclear and Particle Physics Proceedings*, pages 340–346, 2016.

[46] DEAP-3600 Collaboration. The DEAP-3600 Dark Matter Search Experiment. *To be published*, 2017.

[47] Hamamatsu Photonics K.K. Large Photocathode Area Photomultiplier Tubes. electronic, 2016. URL `http://www.hamamatsu.com/resources/pdf/etd/LARGE_AREA_PMT_TPMH1286E.pdf`.

[48] H.M. O'Keeffe. Low Energy Background in the NCD Phase of the Sudbury Neutrino Observatory, 2008.

[49] National Institute of Standards and Technology. ASTAR: stopping-power and range tables for helium ions. URL `http://physics.nist.gov/PhysRefData/Star/Text/ASTAR.html`.

[50] B. Cai, M.G. Boulay, M. Kuzniak, and P. Skensved. DEAP-STR-2011-009 Rev 2: Neutron backgrounds in DEAP-3600. *Internal Document*, 2011.

[51] C.M Nantais, B.T Cleveland, and M.G Boulay. Radiopurity measurement of acrylic for DEAP-3600. *AIP Conference Proceedings*, 1549, 2013.

[52] C.M Nantais. Radiopurity measurement of acrylic for the DEAP-3600 dark matter experiment. MSc Thesis, Queen's University, 2014.

[53] M. Kuzniak. DEAP-STR-2015-002 Rev 1: TPB Manufacturing Instruction and Assay Record. *Internal Document*, 2015.

[54] B. Cai, E. Devoie, C. Jillings, and M. Kuzniak. DEAP-STR-2014-009 Rev 1: DEAP-3600 AV surface backgrounds from radon exposure. *Internal Document*, 2014.

[55] S. Seibert *et al.* Reactor Analysis Tool, 2014.

[56] J. Allison *et al.* Recent developments in GEANT4. *Nuclear Instruments and Methods in Physics Research Section A: Accelerators, Spectrometers, Detectors and Associated Equipment*, 835:1860225, 2016.

[57] B. Beltran, J. Bueno, A. Hallin, and C. Mielnichuk. DEAP-STR-2015-00 Rev 2: Background events from the DEAP-3600 neck components and TPB - a short note. *Internal Document*, 2015.

[58] B. Cai. Private communication with James Bueno (email). October 2015.

A Derivation of estimate for surface contamination of neck hardware

The following discussion of source terms used in this analysis is from [57].

All acrylic surfaces are assumed to be completely clean after sanding under nitrogen purge. During installation of the neck hardware in the detector, exposure of the acrylic to ^{222}Rn in mine air has led to an estimated 0.6 μBq of ^{210}Po activity [58].

The LAr is assumed to be initially free of ^{222}Rn after passing through the activated charcoal trap. Contamination is introduced in the LAr from ^{222}Rn emanation in the welds of the process system. Gaseous ^{222}Rn has a half-life of 3.82 days, which allows the gas to spread evenly through the LAr. The short-lived, non-gaseous daughters then deposit on surfaces in contact with the liquid argon, resulting in a continuous source of alpha particle decays from ^{218}Po and ^{214}Po.

There are an estimated 15 m of welds in the detector: $\sim$ 200 inches of neck welds in contact with the LAr, $\sim$ 200 inches in between the neck vacuum jacket wall and inner neck that is exposed to argon vapour, and $\sim$ 5 m from the 0.5 inch in cooling coil tubing. The emanation chamber at Queen's University reports 5 $\pm$ 1 μBq/m^2 of ^{222}Rn, which translates to a total of 75 μBq for 15 meters of welds.

Alternatively, the contamination can be estimated from DEAP-1. In DEAP-1, 100 μBq of ^{222}Rn was measured through ^{222}Rn-^{218}Po tagging. This contamination is assumed to have entered the detector through welds in the process system. Estimating the surface area of DEAP-3600 to be 10 m^2, the DEAP-1 ^{222}Rn activity results in 10 μBq/m^2 of ^{218}Po and ^{214}Po in DEAP-3600.

The higher DEAP-1 estimate of 100 μBq for ^{218}Po and ^{214}Po, and 0.6 μBq of ^{210}Po contamination are used in this analysis.